

Standardized Images and Evaluation Metrics for Tomography

Anna Frixou ¹, Theodoros Leontiou ^{2,3}, Efstathios Stiliaris ^{1,4}, and Costas N. Papanicolas^{1,4,5*}

¹ The Cyprus Institute, Nicosia, Cyprus.

² Department of Mechanical Engineering, Frederick University, Nicosia, Cyprus

³ Frederick Research Center, Nicosia, Cyprus

⁴ Department of Physics, National and Kapodistrian University of Athens, Athens, Greece

⁵ The Cyprus Academy of Sciences, Letters and Arts

Abstract

Advances in instrumentation and computation have enabled increasingly sophisticated tomographic reconstruction methods. However, existing evaluation practices—often based on simple phantoms and global image metrics—are limited in their ability to differentiate among modern high-fidelity reconstructions. A standardized, quantitative framework capable of revealing subtle yet meaningful differences is therefore required.

We introduce such a framework, built upon two core components. The first is a set of four standardized reference images—Source, Detector, Ideal, and Realistic—each derived from physical modeling and representing a distinct stage in the imaging and reconstruction chain. The second is a suite of diagnostic and quantitative tools that remain sensitive in regimes where conventional metrics (e.g., SSIM, PSNR, NMSE, CC) tend to saturate. These include pixel-wise χ^2 and difference maps, their quantitative characterization, spectral decomposition of intensity distributions, and Region-of-Interest (RoI)-based metrics.

Application of this framework to MLEM and RISE-1 reconstructions using software phantoms demonstrates its ability to expose discrepancies that might elude detection by conventional global metrics. While developed in the context of SPECT, the methodology generalizes to other tomographic modalities, providing a reproducible, interpretable, and physically grounded basis for evaluating reconstruction fidelity in the high-performance regime.

Keywords: Tomography, image reconstruction, reconstruction algorithms, MLEM, RISE, evaluation of reconstruction methods

Preprint. This manuscript is under review at MDPI Tomography and has not undergone peer review.

Received:

Revised:

Accepted:

Published:

Citation: Lastname, F.; Lastname, F.; Lastname, F. Title. *Tomography* **2025**, *1*, 0. <https://doi.org/>

Copyright: © 2026 by the author. Submitted to *Tomography* for possible open access publication under the terms and conditions of the Creative Commons Attribution (CC BY) license (<https://creativecommons.org/licenses/by/4.0/>).

1. Introduction

The quality of tomographic image reconstruction is of fundamental importance in a wide range of fields—from clinical diagnostics in nuclear medicine to structural imaging in industrial and materials science. In recent years, the field has experienced dramatic advances, driven by both improved detector instrumentation and the increasing availability of powerful computational resources. These developments have enabled the use of sophisticated reconstruction methods, including algorithmic, AI-based, and hybrid physics-informed approaches, that operate with high precision and accuracy. As a result, reconstruction techniques are now approaching the limits of what is physically achievable, although the extent of this gap has yet to be clearly quantified.

However, this progress also exposes a critical limitation in how reconstruction performance is currently evaluated. Tomographic image reconstruction is a mathematically

ill-posed inverse problem: for any given set of projection data (e.g., a sinogram), multiple images may exist that are consistent with it. Reconstruction methods differ in how they incorporate assumptions, regularization, or prior knowledge to resolve this ambiguity. Yet the tools typically used to assess reconstruction quality—simple digital or hardware phantoms and global metrics such as Structural Similarity Index Measure (SSIM), Normalised Mean Squared Error (NMSE), Correlation Coefficient (CC), or Peak Signal-to-Noise Ratio (PSNR)—were not designed for this high-performance regime. These traditional metrics tend to saturate in high-quality reconstructions, making it difficult to capture subtle but diagnostically relevant differences, thereby offering limited guidance for further methodological development.

Furthermore, evaluation is often based on a single reference image—typically the “phantom”—which is assumed to represent ground truth. While this approach is widespread, it is conceptually problematic. The phantom defines the object to be imaged, but its detailed structure cannot be reconstructed without prior knowledge, compounding the ill-posedness of the problem. Physical processes such as scattering, attenuation, noise, and imperfect detection introduce distortions that make exact recovery of the true distribution—represented by what we term the “Source Image”—fundamentally impossible. As a result, comparisons made directly against the “Source Image” may lead to misleading conclusions about reconstruction method performance. Instead, we argue that multiple reference images are needed—including an “Ideal image” that represents the best possible reconstruction achievable under perfect acquisition conditions.

These challenges raise a set of fundamental questions:

- What set of reference images should be used to evaluate a reconstruction method in a meaningful and physically realistic way?
- How can we distinguish between methods that perform similarly under traditional metrics?
- How can we detect local deficiencies or residual information when global scores plateau?
- And is it possible to quantify the gap that exists between a given reconstruction and what is physically achievable?

Together, appropriately chosen phantoms and refined quantitative metrics form a robust, structured, and reproducible framework for assessing the performance of reconstruction methods in a physically meaningful way. We demonstrate the utility of this framework through detailed case studies involving the well-established Maximum Likelihood Expectation Maximization (MLEM) algorithm and the novel Reconstructed Image from Simulations Ensemble -1 (RISE-1) method, applied to Shepp-Logan software phantom. While our focus is on Single Photon Emission Computed Tomography (SPECT), the structure of the framework extends naturally to Positron Emission Tomography (PET) with only minor adjustments to the attenuation and coincidence models. Its application to other modalities—such as Computed Tomography (CT), Magnetic Resonance Imaging (MRI), or thermal imaging—is possible in principle, but requires modality-specific definitions of the standardized images and careful adaptation of the underlying forward and noise models. In what follows, we describe the rationale, construction, and application of each element in this evaluation toolkit.

2. Materials and Methods

The overarching goal of tomographic image reconstruction is to obtain a 3-D image depicting aspects of the imaged object as accurately as possible from the obtained experimental data (most often organized in the form of a sinogram). As the tomographic image

reconstruction is mathematically an “ill-posed problem” [1,2], the challenge is to select among the many possible solutions that the sinogram can support, often injecting prior knowledge into the analysis [2].

The use of both software (digital) and hardware phantoms plays a vital role in the development and refinement of image-reconstruction methods [3–6]. The use of phantoms offers a most valuable advantage: the reconstructed image can be directly compared to the known structure of the object being imaged. This in turn necessitates the development and use of metrics that can quantify this comparison. In our efforts to develop new methodologies and enhance existing ones, we found that while established metrics were effective for certain studies, the introduction of new standardized images and phantoms and of new evaluation criteria and methods was particularly valuable. The newly introduced images and metrics reported in this work have broad applicability, which is showcased in two examples:

- a) in evaluating improvement and convergence in the well-known case of the MLEM reconstruction algorithm [7], and
- b) in evaluating the performance of a novel reconstruction algorithm and benchmarking it versus the well-known MLEM.

2.1. *Phantoms:*

In emission tomography, a phantom—whether realized in software or as a physical object—refers to a well-defined arrangement of radioactive emitters (e.g., technetium-99m, ^{99m}Tc) that serve as the source of radiation detected by the imaging system (such as γ -rays in SPECT). This arrangement is characterized by a precisely specified spatial distribution, in two or three dimensions, together with the emission intensity (specific activity) at each location. Invariably, phantoms also include detailed descriptions of surrounding materials—both within and outside the emitting regions—including density, absorptivity, and other properties relevant to the physics of γ -ray propagation. The shape and physical properties, even of non-emitting γ -ray structures (e.g., bone), influence the attenuation and scattering of the emitted γ -rays before they reach the detector.

In this work, we use the term phantom exclusively for this physical or digital configuration, to clearly distinguish it from its “Source Image”—the graphical representation of the radiation-emitting portion of the phantom. Other image-based representations derived from this primary configuration are introduced in Section 2.3.

For our investigation, we employed several phantoms, both standardized and custom-designed. In the results presented here, we focus on a widely used software phantom: the Shepp–Logan [8,9] phantoms which are shown graphically in Figure 1. Variations of these are used throughout the imaging community. Extending the analysis to other phantom designs or to three-dimensional cases is straightforward. The Shepp–Logan phantom extends evaluation to heterogeneous, anatomically inspired structures with smoothly varying intensities.

The second software source phantom used is a two-dimensional Shepp–Logan-like phantom with the typical head structures in the form of ellipsoids with variable size and activities. In the modified version used in this work, the cranial bone has been removed, while the major large ellipsoid representing the brain grey and white serves also as a background source. Geometrical details and source activities of the modified Shepp–Logan phantom are shown in Table 1. SRC0 is a background water source; (SRC3–SRC8) have the same and four times the specific activity of the two bigger ellipsoids SRC1 and SRC2. Table 1 summarizes the geometric and activity parameters of the modified Shepp–Logan phantom.

Source	Position [mm]	Minor X Axis [mm]	Major Y Axis [mm]	Angle ϕ [deg]	Surface / π [mm 2]	Surface [a.u.]	Activity [kBq]	Specific Activity [kBq/a.u.]
SRC0	(0,0)	75	100	0°	7500.00	1200	6000	5
							24000	20
SRC1	(+24,+2)	12	34	-18°	408.00	65	325	5
SRC2	(-24,+2)	17	45	+18°	765.00	122	610	5
SRC3	(0,+40)	23	27	0°	621.00	100	1000	10
SRC4	(0,+13)	5	5	0°	25.00	4	40	10
SRC5	(0,-11)	5	5	0°	25.00	4	40	10
SRC6	(-11,-64)	5	2.5	0°	12.50	2	20	10
SRC7	(0,-64)	2.5	2.5	0°	6.25	1	10	10
SRC8	(+9,-64)	2.5	5	0°	12.50	2	20	10

Table 1. Description of the radiation-emitting areas of the Shepp–Logan phantom consisting of eight ellipsoids (SRC1–SRC8) of various sizes and activities.

The specific activity distributions of the Shepp–Logan phantom is shown graphically in Figure 1.

2.2. Evaluation of Reconstruction Algorithms in Medical Imaging

Reconstruction algorithms across a range of imaging modalities are routinely assessed both in absolute terms and through comparative analysis, with a focus on their fidelity in reproducing the underlying imaged object. These evaluations are typically performed using a combination of physical and digital (software) phantoms, which serve as “ground-truth” references. The reconstructed images are quantitatively compared to the known structure of these phantoms using a suite of established and well-characterized metrics. These metrics are designed to quantify various aspects of image quality, such as spatial resolution, contrast recovery, and noise characteristics. In Section 3, we will explore in detail the extent to which these metrics effectively capture the reconstruction performance of a given methodology, and how reliably they discriminate between alternative reconstruction methods.

Despite the apparent maturity of this evaluation framework, several important questions remain open. For instance, is it theoretically possible for any reconstruction methodology to perfectly reproduce a source phantom given ideal conditions? If not, what fundamental limitations—whether physical, computational, or methodological—define the closest achievable approximation? Furthermore, when two reconstruction methodologies yield comparably high metric scores, it remains unclear whether this indicates genuine equivalence in performance, a saturation point dictated by physical constraints, or merely a shortcoming in the sensitivity of the employed evaluation metrics. It is plausible that both limitations of the metrics and physical asymptotes in performance play a role. In the subsequent sections, we aim to investigate these questions and offer at least partial answers supported by theoretical insights and empirical evidence.

Central to this inquiry is the availability of highly advanced simulation frameworks that enable precise modeling of the underlying physical processes in imaging. In particular, the Monte Carlo-based GEANT4/GATE software suite [10,11] has emerged as an indispensable tool in nuclear-medicine imaging modalities. Its capability to simulate complex interactions of particles or photons with matter at high accuracy, combined with the increasing affordability of intensive computational resources, provides a powerful foundation for probing the ultimate limits of image-reconstruction accuracy in SPECT and PET modalities. These tools allow for the generation of controlled, high-precision datasets, which are critical for disentangling methodological limitations from intrinsic physical constraints.

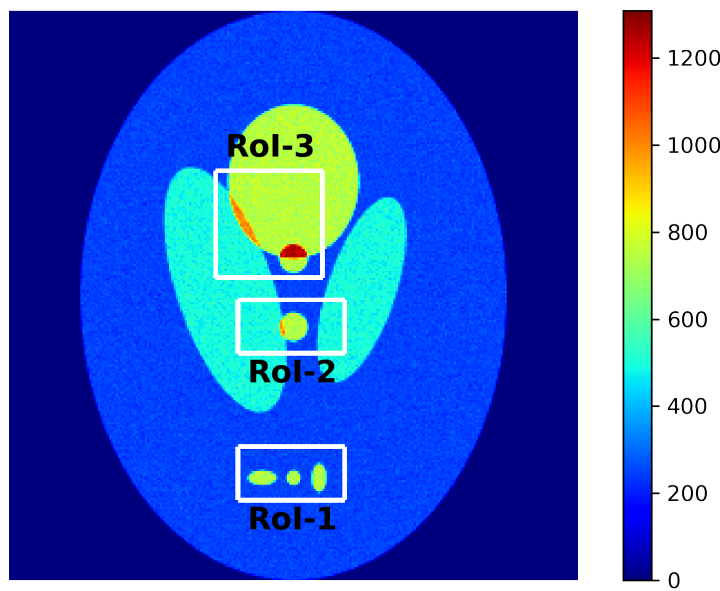


Figure 1. Graphical representation of the specific activity of the two-dimensional "Source Images" of the Shepp-Logan phantom. Selected Regions of Interest (RoIs) are shown and will be discussed at Section 2.4.3.

For Shepp-Logan phantom, SPECT image results of simulation presented in this paper were produced using the Monte Carlo GEANT4/GATE [10,11] software package together with a typical γ -camera dual-head system routinely used in a clinical environment and radio-tracer ^{123}I with γ -rays at 159 keV. The phantoms are constructed using the simple analytical functions allowed by GATE, with the characteristics shown in Table 1. Since our study focuses on the reconstruction quality of the central-slice image only, a natural thickness of ± 5 mm is given to the phantom geometry. A total of 128 planar images are acquired with this simulated γ -camera system, corresponding to an angular step of $\Delta\theta=2.8125^\circ$, covering the full 360° range. The obtained phantom matrices and the generated sinograms are normally composed to a 256×256 pixel image size, unless otherwise specified.

2.3. The need for standardized images

While the foundational principles of tomography were established [12] and significant early advances were achieved [13] in an era predating modern computing, the ability to incorporate detailed, physics-based modeling of all relevant processes influencing image formation was severely limited. Early methodologies often relied on drastic simplifying assumptions, as the computational tools necessary for realistic simulations did not yet exist. Today, however, the field benefits from highly accurate and comprehensive simulations, capable of modeling even subtle effects that impact the quality of the reconstructed image. These include inhomogeneities in absorption due to variations in the material between the source and detector, scattering phenomena, and differences in imaging geometry or detector response.

As a result, the reconstructed image—and its corresponding sinogram—can vary depending on the specific assumptions and physical models used in the simulation. Rather than treating this variability as a limitation, it offers an opportunity: these simulation-derived variants can serve as new reference standards against which to compare the outputs of reconstruction methodologies under evaluation. Such comparisons provide a

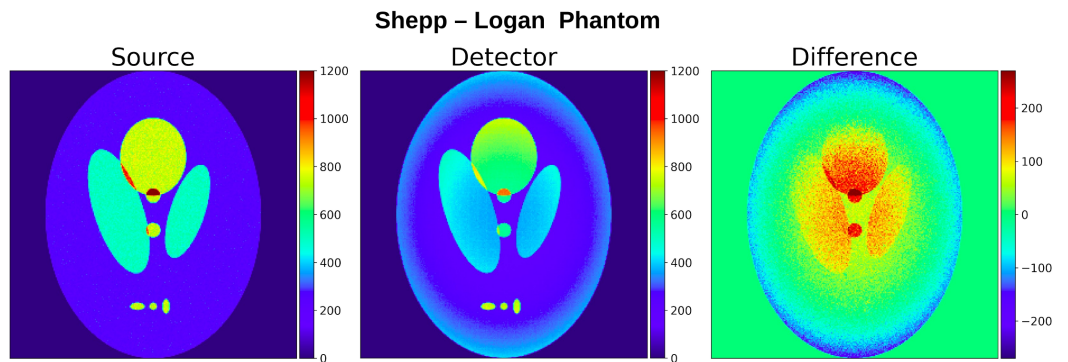


Figure 2. Source and Detector images from simulations of the modified Shepp–Logan phantom. The "Source Image" includes all emitted photons; the Detector image includes only detected ones. The rightmost panels show their difference; photon absorption within the phantom is the dominant effect.

more nuanced and realistic benchmark for methodology performance, grounded in the complex physical realities of image formation.

A simple image that is produced by simulating in detail the processes that occur from emission to detection is what we term the "**Detector Image**", which is constructed by using the nominal position of the emitted photons that were detected. Figure 2 shows the images of the source phantom and of the detector image for the two test phantoms used in our study and the difference among them.

A widely used reconstructed image obtained using detailed simulation packages is the image that is expected to emerge from a realistic detection system—e.g., a commercial scanner. In such simulations the detailed specification of a digital or hardware source phantom and every detail of the detection system is meticulously described. This image, which we term the "**Realistic Image**", is particularly useful for field applications—for example, in a clinic or a laboratory that relies on a specific detection setup and equipment to derive its results. The "Realistic Image" is the appropriate tool in such environments to explore issues such as optimization of radiopharmaceutical dose (in PET or SPECT), collimator geometry (in SPECT), number of planar images to be taken, and similar parameters. However, it is of limited use in assessing the capabilities and performance of a reconstruction methodology, as discussed above. To facilitate this need we propose the introduction of the "**Ideal Image**".

In practical imaging scenarios, no matter how advanced the reconstruction methodology is, the resulting image will never reach a statistically perfect representation of the source phantom. This is due to several limiting factors:

- The interaction of the emitted photons within the body containing the volume to be imaged (e.g., a patient's body), including scattering, annihilation, or kinematic blurring (in PET), some of which are often grouped under the encompassing term *attenuation*.
- The interaction of the photons with intervening material between the boundaries of the imaged object and the detector array (e.g., air, collimator, and encasing materials in SPECT).
- Limitations of detection such as finite angular acceptance or energy resolution.
- Limitations in data acquisition, including finite number of projections and limited counting statistics.
- Electronic noise and uncertainties in the instrumentation chain leading to event recording.
- Uncertainties introduced in analyzing finite-statistics digitized data (e.g., binning errors).

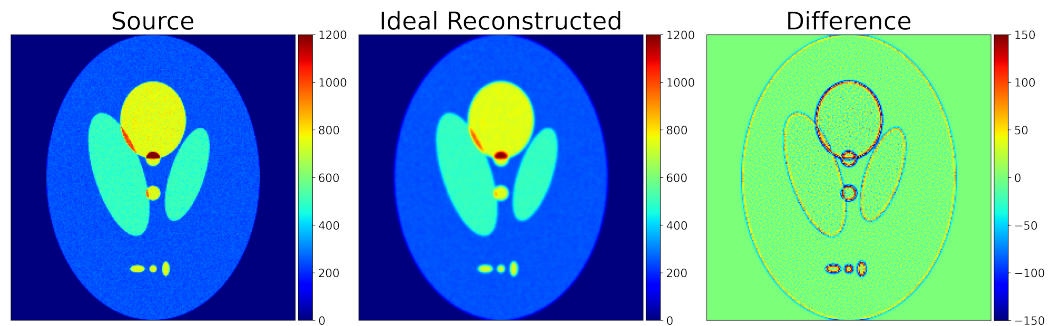


Figure 3. Simulated Shepp-Logan image of the “Source Image” and the “Ideal Image”, together with their difference.

Many of these limitations can be mitigated—for example, case (d) by acquiring a sufficiently large number of projections and allowing extended counting times to ensure robust statistics. With the exception of case (a), this strategy applies broadly. The image resulting from such a simulation—conducted under near-ideal conditions—is what we define as the “**Ideal Image**”. This image represents the highest level of accuracy attainable by any reconstruction methodology and thus serves as an absolute benchmark against which practical reconstruction methods can be evaluated. In this sense, the “**Ideal Image**” is universal: it is independent of specific detection geometry, equipment, or algorithm, and is determined solely by the fundamental physics and statistical constraints of the imaging system.

In order to address the issue of minimizing the effects deriving from the geometric and construction peculiarities of the collimator—a very important consideration in SPECT due to finite angular acceptance—the concept of the “**ideal collimator**” was introduced. In imaging systems like SPECT, collimators are made of dense, absorbing materials that allow only rays traveling in specific directions to reach the detector. However, collimators are not infinitely narrow, which introduces blurring: some rays scatter on or penetrate through the collimator and reach neighboring detector channels. In simulations, a software collimator ignores the finite thickness of a hardware collimator and allows each channel to collect rays from a single direction. An “ideal collimator” is therefore effectively a software filter that accumulates only rays emitted perpendicularly to the detector surface. Differences between the image of the phantom and the “Ideal Image” thus reflect inherent deterioration of the image due to (a) above, which no reconstruction methodology can overcome without the use of prior-knowledge input. Such a comparison is shown in Figure 3. Differences between the image derived through a reconstruction methodology and its corresponding “Ideal Image” are attributable to deficiencies in the reconstruction methodology. Quantifying these differences or deficiencies will be the topic of the following section. Table 2 summarizes the four types of images we introduced, along with the method of generation and principal utility.

This taxonomy is not merely conceptual: it follows directly from the structure of the physical forward model used in SPECT and other tomographic modalities. The “Source Image” represents the emissivity term; the “Detector Image” represents, with high fidelity, the emission and detection physics underlying the process; the “Ideal Image” corresponds to the forward model stripped of instrumental imperfections and noise; and the “Realistic Image” incorporates all real system effects. These four images therefore isolate distinct physical contributions—source distribution, propagation physics, detection characteristics, and acquisition statistics—and are essential for disentangling algorithmic limitations from physical constraints. In this sense, the taxonomy is required for any rigorous, physics-grounded evaluation of reconstruction fidelity.

Table 2. The four images and sinograms defined and used in this work.

Image/Sinogram	Generation Method	Comments
Source	Direct emissivity map of the phantom. No attenuation, scatter, or detector effects; no forward model needed.	Provides the reference “reality” and a benchmark for testing reconstruction methodologies.
Detector	Forward model accounts for attenuation, scatter, geometric acceptance, and detection efficiency. Provides an excellent representation incorporating all detection physics.	Represents the starting point for any reconstruction; reconstructed images should improve upon the Detector Image.
Ideal	Forward model under asymptotic conditions: infinite statistics, ideal collimator, no detector blur. Represents the physical upper bound on recoverable information.	Provides an absolute benchmark for testing reconstruction methodologies.
Realistic	Forward model with full system effects: finite resolution, collimator blur, detector response, and realistic counts. Represents actual scanner behavior.	Useful for field applications (e.g., clinics or laboratories) that rely on specific detection equipment to derive results.

The method of their generation and their principal utility is listed in the table. They are discussed in a more thorough manner in the text.

2.4. Quantitative and Diagnostic Evaluation Tools

As outlined in the preceding discussion, the development and validation of novel image reconstruction methodologies necessitate the use of well-characterized, standardized benchmarks, along with robust and meaningful quantitative metrics. Such benchmarks are essential to ensure objective, reproducible, and interpretable evaluations of performance. The standardized images defined in Section 2.3 — Source, Detector, Ideal, and Realistic — provide the physically meaningful anchors needed to evaluate fidelity across image and sinogram domains. These images establish a structured framework against which reconstructed outputs can be compared. In the present section, we extend the evaluation methodology by

- (i) recalling the global quantitative metrics that remain essential for baseline comparisons,
- (ii) introducing local and spectral diagnostics that retain sensitivity when global measures saturate, and
- (iii) formalizing Region-of-Interest (RoI) analysis as a focused evaluation tool.

The section concludes with an integrated interpretation framework that unifies all these approaches.

In Table 3 metrics and evaluation criteria used in our investigations are presented. For the well-established ones, references are provided, while those introduced in this work they are marked as “new”.

2.4.1. Global quantitative metrics

Several well-established quantitative metrics are routinely employed to assess the quality of reconstructed sinograms and images and their fidelity to reference data. These metrics are applicable to both reconstructed images and sinograms and are instrumental in benchmarking methodological performance.

Table 3. Applicability of evaluation metrics and diagnostic tools across different imaging contexts

Metric	Software Phantom	Hardware Phantom	Field Data	References
Correlation Coefficient (CC)	✓	✓	Only on sinograms	[14,15]
Normalized Mean Square Error (NMSE)	✓	✓	Only on sinograms	[16]
Peak Signal-to-Noise Ratio (PSNR)	✓	✓	Only on sinograms	[17]
Contrast-to-Noise Ratio (CNR)	✓	✓	Only on sinograms	[18]
Structural Similarity (SSIM)	✓	✓	Only on sinograms	[19]
χ^2 maps of sinograms	✓	✓	✓	new
χ^2 maps of images	✓	✓	✗	new
Difference map of sinograms and SCI	✓	✓	✓	new
Difference map of images and SCI	✓	✓	✗	new
Sinogram Spectral Decomposition Comparison and spectra $\chi^2_{reduced}$ of "Ideal" and reconstructed image.	✓	✓	✓	new
Image Spectral Decomposition Comparison and spectra $\chi^2_{reduced}$ of "Ideal Sinogram" and the one resulted from a reconstruction.	✓	✓	✗	new

(✓) indicates conditional or partial applicability; (✗) indicates the metric cannot be meaningfully applied in that setting. For "field" (experimental or clinical) data, image-based comparisons often require projections to sinogram space.

Global metrics often condense image or sinogram agreement into a single, reproducible number such as χ^2 . They are easy to report and compare but can mask localized or structured residuals once reconstructions are already of high quality. We therefore use them as a baseline, and subsequently probe deeper with the diagnostics presented in Sections 2.4.2 and 2.4.3. For the sake of completeness, accuracy, and reproducibility, we provide both references (see Table 3) and the exact formulas employed below.

Let $X, Y \in \mathbb{R}^N$ denote vectorized reconstructed and "Ideal" images (or sinograms) respectively, with means μ_x, μ_y , variances σ_x^2, σ_y^2 , and covariance σ_{xy} . All sums are over valid pixels or bins.

1. Correlation Coefficient (CC)

The correlation coefficient evaluates the degree of linear similarity between two datasets—typically, the reconstructed image and the reference image:

$$CC = \frac{\sum(X - \mu_x)(Y - \mu_y)}{\sqrt{\sum(X - \mu_x)^2 \sum(Y - \mu_y)^2}}$$

2. Normalized Mean Square Error (NMSE)

This metric quantifies the overall squared deviation between a reconstructed image or sinogram and its reference, normalized by the square of the reference image:

$$NMSE = \frac{\sum(X - Y)^2}{\sum Y^2}$$

3. Peak Signal to Noise Ratio (PSNR)

PSNR measures the ratio between the maximum signal intensity and the mean-square reconstruction error:

$$\text{PSNR} = 10 \log_{10} \left(\frac{\text{MAX}_X^2}{\text{MSE}} \right)$$

where $(\text{MAX}_X)^2$ is the maximum possible pixel value of the reconstructed image and MSE is the Mean Squared Error of it. ($\text{MSE} = \sum(X - Y)^2 / N$, N = number of valid pixels.)

4. Contrast to Noise Ratio (CNR)

CNR assesses the detectability of a target against background noise. It is defined as:

$$\text{CNR} = \frac{T - B}{\sigma_B}$$

where T is the average reconstructed value in the target area, B is the average, and σ_B is the standard deviation of image elements corresponding to the background area.

5. Structural Similarity Index (SSIM)

SSIM measures the structural fidelity between two images by combining luminance (l), contrast (c), and structure (s) components:

$$\text{SSIM} = l \cdot c \cdot s$$

$$l = \frac{2\mu_X\mu_Y + C_1}{\mu_X^2 + \mu_Y^2 + C_1}, \quad c = \frac{2\sigma_X\sigma_Y + C_2}{\sigma_X^2 + \sigma_Y^2 + C_2}, \quad s = \frac{\sigma_{xy} + C_3}{\sigma_x\sigma_y + C_3}$$

Here C_1, C_2, C_3 are small constants preventing division by zero. SSIM values near 1 indicate close similarity; deviations from unity signify structural differences not captured by simpler intensity-based metrics.

6. Global Scalar Metrics

Global scalar metrics remain widely used in tomographic image analysis because they condense the agreement between two images or sinograms into a single reproducible quantity. In principle, many such metrics may be employed to evaluate reconstruction fidelity. Beyond the classical chi-square statistic, we have examined a broader family of global comparison measures, including information-theoretic divergences such as the Jensen–Shannon (JS) divergence [20,21] and the Kullback–Leibler (KL) divergence [22]; statistical–geometric measures such as the Hellinger distance [23]; and optimal-transport distances such as the 1-Wasserstein and 2-Wasserstein metrics [24–26]. These modern alternatives often retain sensitivity in high-fidelity regimes, where conventional scalar metrics (e.g., SSIM, NMSE, CC, PSNR) tend to saturate and lose discriminative power.

On the role of metrics as cost functions.

Many of these comparison metrics are not only used for evaluation purposes but also frequently serve as cost functions guiding the reconstruction process itself. Iterative and model-based algorithms often optimize a specific discrepancy measure—whether a likelihood-based statistic such as the chi-square, an information divergence such as the Kullback–Leibler divergence, or a geometric discrepancy arising from optimal transport. The choice of cost function thus strongly influences convergence behavior, noise propagation, and the types of structures preferentially preserved or suppressed. The optimal choice depends on the physical acquisition model, statistical noise characteristics, and diagnostic priorities of the imaging modality. In this respect, although more sophisticated metrics can offer improved sensitivity or robustness, simpler measures such as the chi-square retain practical advantages in transparency, physical

grounding, and broad applicability across imaging and sinogram domains.

Rationale for the use of chi-square in this work.

For the purposes of this manuscript, we have deliberately adopted the chi-square statistic as the primary global scalar metric. This decision reflects considerations of interpretability, methodological consistency, and reproducibility across all reconstruction scenarios examined in this study, rather than an assertion of its superiority over alternative metrics. The chi-square metric provides a physically grounded, noise-aware measure of discrepancy and can be uniformly applied in image, sinogram, and spectral comparisons within our evaluation framework.

Formally, given two arrays (X) and (Y) representing reconstructed and reference data (image or sinogram) and corresponding variance estimates (σ_i^2), the global chi-square metric is defined as: $\chi^2 = \sum_i \frac{(X_i - Y_i)^2}{\sigma_i^2}$, where the sum extends over all valid pixels or bins. When explicit variance estimates are unavailable, reduced or unweighted chi-square variants may be used, though their interpretation becomes less strictly statistical.

These global scalar metrics, collectively, provide a necessary quantitative foundation for evaluating reconstruction methodologies. However, once their values saturate—especially for metrics such as the Structural Similarity Index and the Correlation Coefficient—their discriminative power diminishes. The next subsections therefore introduce local and spectral diagnostics that remain sensitive in this regime.

These global metrics, collectively, provide a necessary quantitative foundation for evaluating reconstruction methodologies. However, once their values saturate—especially for SSIM and CC—their discriminative power diminishes. The next subsections therefore introduce local and spectral diagnostics that remain sensitive in this regime.

In all χ^2 evaluations presented in this work, the variance entering the denominator is derived directly from the Monte-Carlo simulation and is therefore dominated by counting statistics. The underlying signal is taken as noise-free. The χ^2 used throughout is the reduced chi-square, computed either globally or pixel-wise to form χ^2 maps.

Pixel independence cannot be assumed in sinograms or reconstructed images, since both contain spatially correlated structures. For this reason, χ^2 is used as a discrepancy measure and as a reconstruction cost function, but not for estimating parameter uncertainties; those are obtained with the Jackknife method. The choice of χ^2 reflects simplicity and transparency, not exclusivity: other discrepancy metrics were examined, and the qualitative conclusions reported here do not depend on the particular cost function. As noted elsewhere, the optimal choice of discrepancy metric is modality- and application-dependent.

2.4.2. Local and Spectral Diagnostic Tools

Motivation

Global metrics (Section 2.4.1) provide indispensable, reproducible scalar summaries of agreement between reconstructed and reference data. However, in the high-fidelity regime reached by modern methodologies, these metrics often reach asymptotic behavior (e.g., global χ^2 values) or saturate (e.g., $\text{SSIM} \approx 1$, $\text{NMSE} \approx 0$), concealing where residual discrepancies remain and whether those residuals are random or contain structured information that can still be recovered.

To overcome this limitation, we employ a set of spatial and spectral diagnostics designed to (i) expose localized deviations, (ii) evaluate their statistical significance, and (iii) determine whether the residuals are organization-free (noise-like) or structurally coherent (information-bearing). These diagnostics are applied both in image and sinogram domains, using the standardized images introduced in Section 2.3.

1. χ^2 and Image-Difference Maps

Image-difference maps and χ^2 maps serve as valuable diagnostic tools, providing spatially resolved insight into how reconstructed data compare with a reference image or sinogram. Difference maps highlight pixel- (or voxel-)wise discrepancies, allowing structural mismatches to be identified in images and projection-space inconsistencies to be detected in sinograms. χ^2 maps extend this concept by normalizing residuals against expected noise variance, thereby yielding a statistically grounded measure of local agreement. Whereas image-difference maps emphasize absolute deviations, χ^2 maps account for noise and experimental variability and are particularly useful in iterative methodologies in which χ^2 minimization serves as the cost function.

As a reconstruction converges toward a correct solution, both difference and χ^2 maps should approach zero values across the field of view, with residuals persisting only in regions where reconstruction remains imperfect. Figure 4 illustrates these tools using the Shepp-Logan phantom. In both image and sinogram space, the reconstructed data are compared against their respective references, with the resulting difference and χ^2 maps clearly delineating regions of mismatch. Such visualizations are invaluable for qualitatively diagnosing convergence behavior and guiding methodological refinement.

Formally, let X and Y be two arrays of the same shape representing, respectively, the reconstructed object (image or sinogram) and the reference (typically the "Ideal" Image or sinogram; for field data, the comparison may be performed in sinogram space). Define the residual (difference) map as

$$R = X - Y \quad \text{or} \quad R = |X - Y|,$$

The signed form visualizes the direction of deviations; the absolute form emphasizes magnitude.

To assess the statistical significance of residuals, the pixel-wise (or bin-wise) χ^2 map is computed as

$$\chi^2 = \sum_{i=1}^N \frac{(X_i - Y_i)^2}{\sigma_i^2}$$

Spatially correlated clusters of elevated indicate modeling inadequacies or systematic reconstruction bias, even when the global χ^2 is acceptable.

When χ^2 is the cost function minimized during reconstruction, these maps reveal where the optimization converges effectively and where significant structure remains—information that a single global number cannot convey.

2. Structure & Contrast Index (SCI)

While visual inspection of image-difference and χ^2 maps is a particularly valuable tool for refining reconstruction methodologies, a quantitative assessment can be obtained by applying a new index, the SCI—the product of the structure and contrast components of the Structural Similarity Index (SSIM).

The luminance component of SSIM is not meaningful in this context; its diminishing contribution renders the full SSIM metric unsuitable for evaluating reconstruction quality. Based on our findings, we conclude that SCI is a most sensitive and reliable measure, and we therefore adopt it throughout the remainder of this paper as it provides a precise indicator of structural fidelity.

The values of SSIM and its components for the difference maps of images and sinograms shown in Figure 4 are given in Table 4. The vanishing SSIM and luminance values confirm their lack of relevance. By contrast, the structure and contrast components exhibit discriminative power, indicating their possible role in providing a

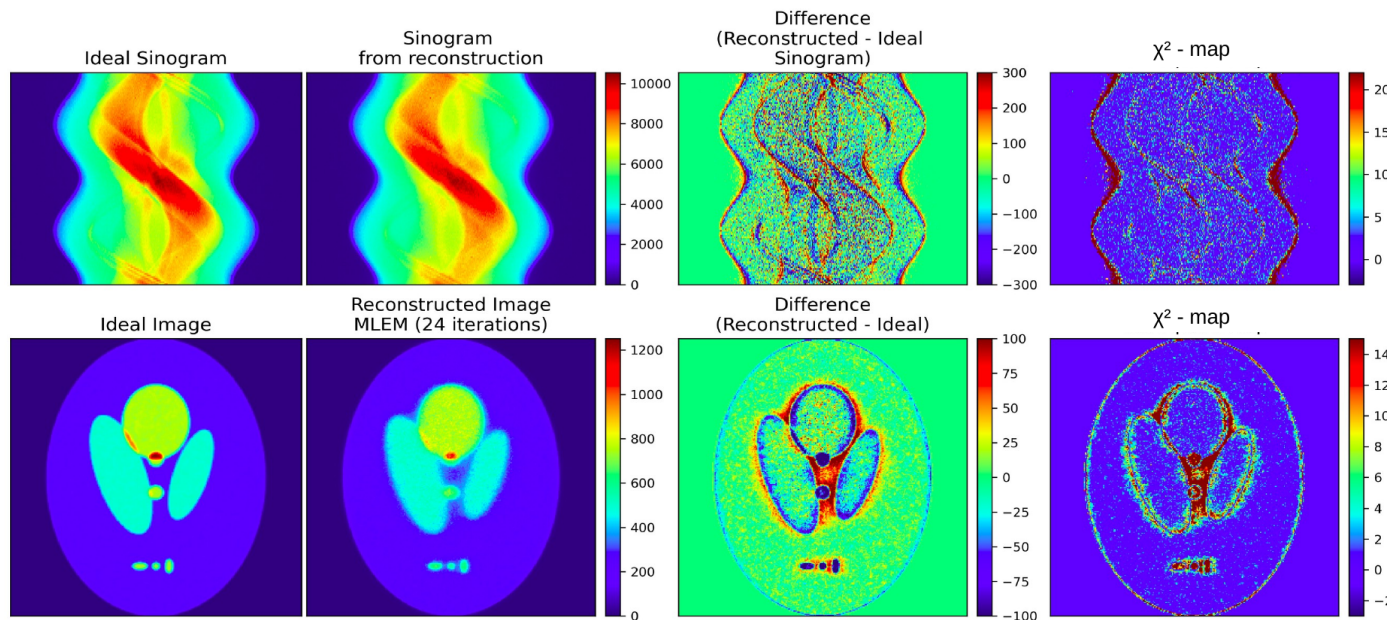


Figure 4. Difference and χ^2 map of images and sinograms. In the first row, the sinogram corresponding to an “Ideal Image” of a Shepp-Logan phantom and the sinogram resulting from an MLEM reconstruction are shown along with the resulting sinogram difference and χ^2 map. In the second row, the “Ideal Image” from a Shepp-Logan phantom, the MLEM reconstructed image, their difference and the corresponding χ^2 map are shown.

quantitative measure. Their product, captured in the SCI, provides the desired metric, which is also not prone to misrepresenting the situation in cases where one of the two shows insensitivity.

Its diagnostic value is further exemplified and highlighted in Case Study A (Section 3.1), where improvements in MLEM reconstructions are tracked as a function of iteration count.

Low SCI (near the null baseline obtained by randomizing residual phases or by comparing R to white-noise surrogates) indicates residuals are noise-like—little organized information remains. High SCI indicates structured residuals (edges, textures, repeated patterns), implying opportunities for methodological improvement such as better system modeling, regularization tuning, or physics-informed priors.

SCI can be computed in both image and sinogram space. For field data, where ground-truth image structure is unknown, SCI is most reliably applied in sinogram space, where projection-domain statistics are well defined.

Context	SSIM	Luminance	Contrast	Structure	SCI
Sinograms (Difference)	$0.0000 \pm 4 \cdot 10^{-6}$	$0.0000 \pm 4 \cdot 10^{-4}$	$0.07 \pm 2 \cdot 10^{-2}$	$0.13 \pm 4 \cdot 10^{-2}$	$0.009 \pm 4 \cdot 10^{-3}$
Images (Difference)	$0.0000 \pm 6 \cdot 10^{-6}$	$0.0000 \pm 1 \cdot 10^{-4}$	$0.234 \pm 1 \cdot 10^{-3}$	$0.242 \pm 3 \cdot 10^{-3}$	$0.0566 \pm 7 \cdot 10^{-4}$

Table 4. Structural Similarity Index (SSIM), Structure & Contrast Index (SCI), and their components applied to difference maps of sinograms and images shown in Figure 4.

3. **Spectral (Intensity) Decomposition** As an additional diagnostic tool, we introduce the concept of spectral decomposition of tomographic images and sinograms. This approach involves analyzing the intensity content of an image or sinogram—effectively

decomposing it into its spectral components—and comparing the resulting spectral profiles between experimental data and reconstructions.

Given two images X and Y , we first normalize them by dividing each image by its mean intensity:

$$X_{norm} = \frac{X}{mean(X)} \quad Y_{norm} = \frac{Y}{mean(Y)}.$$

With this normalization, the total luminosity of the images becomes comparable, since

$$\sum_i X_{norm}^i = \sum_i Y_{norm}^i.$$

Let S_X and S_Y denote their corresponding intensity distributions, represented as one-dimensional histograms using a common set of NB bins. All bins have the same width and span the full intensity range required to cover both normalized images. A direct comparison of the two histograms is now possible. Their difference can be quantified in a straightforward way by computing the reduced χ^2_{red} value applied to all histogram bins:

$$\chi^2_{red} = \frac{\sum_{i=1}^{NB} (S_X^i - S_Y^i)^2}{NB}.$$

Such comparisons can offer quantitative and visual insight into the fidelity of the reconstruction, particularly with regard to resolution and structural detail. Reconstructions that exhibit blurring typically show broader or attenuated peaks in their spectral histograms, especially in regions corresponding to high-intensity features such as sharp edges or small hotspots.

Conversely, a well-resolved reconstruction preserves the higher-intensity components present in the original image or sinogram. Spectral decomposition thus complements traditional pixel-domain metrics by probing the intensity (frequency) domain, where differences in texture, contrast, and resolution become more apparent.

This can be especially revealing for identifying systematic degradation or smoothing introduced by regularization or filtering within the reconstruction pipeline.

Figure 5 provides representative examples of such spectral histograms for experimental and reconstructed images and sinograms of Figure 4. As illustrated, deviations in the shape and width of the peaks serve as indicators of the degree to which spatial detail has been preserved or lost during reconstruction.

2.4.3. Region-of-Interest (RoI) Analysis

A Region-of-Interest (RoI) is a diagnostic construct that enables localized quantitative evaluation of reconstruction performance within selected sub-regions of an image [27–33].

Conceptually, it functions as a controlled zoom-in on areas of particular diagnostic or structural importance, allowing quantitative scrutiny of features that may be diluted or concealed in global analyses.

By restricting evaluation to meaningful subregions—such as boundaries, isolated hot spots, or regions containing closely spaced sources—RoIs provide a refined perspective on reconstruction quality and help identify local variations that may not be captured by whole-image metrics.

Although an RoI is defined and processed as an image mask, it is not an additional image type but rather a flexible analytical tool within the evaluation framework.

RoIs are defined on any reference image—e.g., the "Ideal Image"—and are subsequently applicable to all standardized images introduced in Section 2.3 (Source, Detector, Ideal, Realistic) that represent the same imaged object or phantom. The same RoI bound-

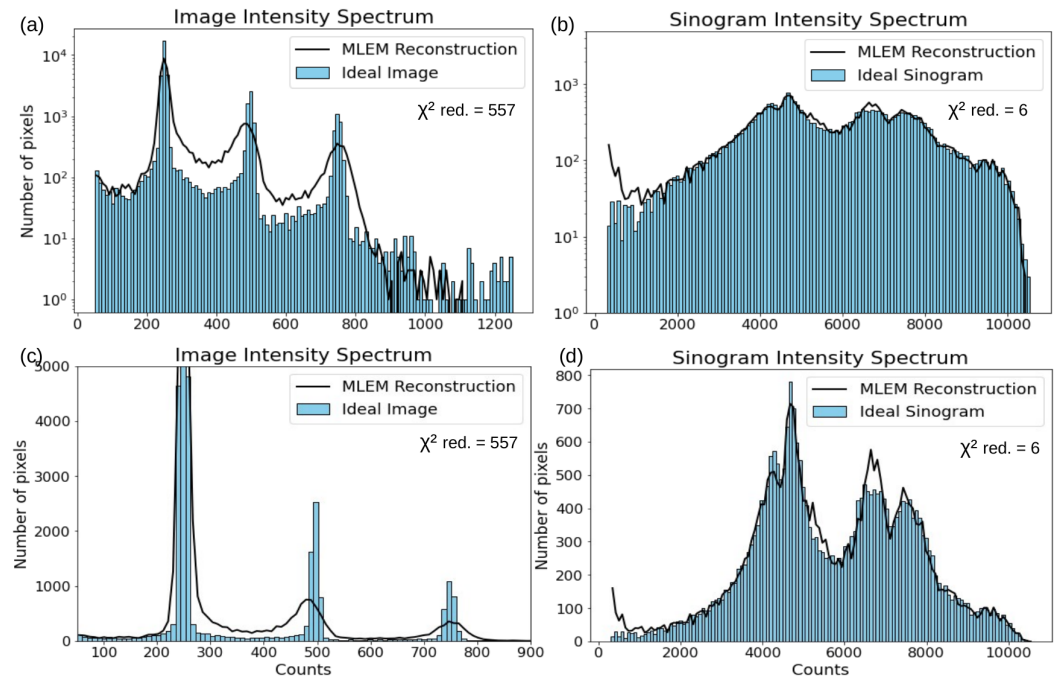


Figure 5. The spectra (on logarithmic scale) of ideal and reconstructed images (a) and sinograms (b) of Figure 4 for the case of MLEM after 24 iterations are provided. The spectra (on linear scale) of ideal and reconstructed images (c) and sinograms (d) of Figure 4 are provided.

aries are then applied identically to each reconstruction to ensure reproducibility and strict comparability among methodologies.

Because RoIs are defined purely in image space, they have **no corresponding sinogram**, underscoring that they operate as diagnostic tools rather than data representations. Each ROI is represented as a binary mask

$$\Omega \subset \mathbb{Z}^n,$$

where denotes Ω the set of discrete pixel or voxel coordinates belonging to the ROI, and \mathbb{Z}^n represents the n -dimensional integer lattice of the image grid (for planar and for volumetric data). Within each ROI, the quantitative metrics introduced in Sections 2.4.1 and 2.4.2 can be recomputed to yield localized indicators of fidelity, for example

$$\text{SSIM}_\Omega, \text{CNR}_\Omega, \text{NMSE}_\Omega, \chi^2_\Omega.$$

These localized metrics quantify reconstruction accuracy exactly where it matters most, avoiding the averaging effects that can obscure deficiencies in global assessments. The selection of RoIs should be guided by the physical or diagnostic objectives of the study.

Edge-crossing RoIs evaluate boundary sharpness and partial-volume effects; hot-spot RoIs assess localized intensity recovery; and regions containing closely spaced structures probe spatial resolution.

Additional RoIs may be defined in uniform or background areas to characterize noise properties or to serve as internal normalization references.

When applied systematically, ROI analysis exposes method-dependent differences that remain invisible to global metrics. For instance, two reconstructions may achieve comparable global SSIM but differ markedly in localized SSIM or χ^2 values within critical subregions—highlighting differences in modeling or regularization performance.

Thus, ROI analysis serves as an integral “magnifying lens” within the quantitative evaluation toolkit, bridging global metrics and local diagnostics to provide a coherent, multiscale view of reconstruction quality.

Figure 1 illustrates representative RoIs used in this work. For the Shepp–Logan phantom, three RoIs are shown: (i) an edge-region ROI probing spatial resolution, (ii) a hot-spot ROI assessing local intensity recovery, and (iii) a uniform-background ROI quantifying noise stability.

The same masks were applied identically to all reconstructions to ensure reproducibility and facilitate direct comparison between methodologies.

2.4.4. Methods of Reconstruction

Two reconstruction methods were employed in this study to demonstrate and validate the proposed evaluation framework: the **Maximum Likelihood Expectation Maximization (MLEM)** [34] algorithm and the recently developed **Reconstructed Image from Simulations Ensemble-1 (RISE-1)** method [35–38].

The former represents a well-established, iterative maximum-likelihood approach, while the latter is a novel stochastic, model-based technique that explores a broader parameter space through ensemble sampling.

Maximum Likelihood Expectation Maximization (MLEM)

The MLEM algorithm estimates the activity distribution f_j that maximizes the likelihood of the measured projections g_i , given the system response matrix P_{ij} . Iterations were performed until convergence, as determined by the stabilization of the global χ^2 between successive reconstructed images.

$$f_j^{(k+1)} = f_j^{(k)} \frac{1}{\sum_i P_{ij}} \sum_i P_{ij} \frac{g_i}{\sum_m P_{im} f_m^{(k)}},$$

where $f_j^{(k)}$ is the estimated value of voxel j at iteration k .

MLEM reconstructions were generated using synthetic projection data simulated with the GATE (Geant4 Application for Tomographic Emission) toolkit under conditions replicating realistic detector geometry and noise statistics.

Reconstructed Image from Simulations Ensemble (RISE-1)

The RISE-1 method, part of the RISE suite, is a stochastic, simulation-driven reconstruction technique that generates a set of statistically consistent candidate images by sampling the space of physical and statistical parameters describing the imaging system. Each ensemble member is obtained by forward-modeling photon transport through the system using the same GATE-based configuration as MLEM, followed by comparison between simulated and measured projections using a χ^2 cost function. The final reconstructed image is calculated as the expectation value over the accepted ensemble members, yielding an inherently regularized solution that suppresses noise amplification and reduces dependence on initial conditions.

Both reconstruction methods were applied to the standardized phantom data introduced earlier. For MLEM, reconstructions were generated at successive iteration counts to analyze convergence behavior and to demonstrate the sensitivity of the proposed metrics and diagnostic tools to subtle image improvements. For RISE-1, the reconstruction was performed using the same projection data and imaging geometry, enabling direct quantitative comparison with the MLEM results.

3. Results

In this section, we demonstrate the utility and versatility of the standardized reference images, simulated sinograms, and evaluation metrics introduced in the previous section. Designed for broad applicability, these tools enable rigorous, quantitative comparison across diverse reconstruction methodologies and imaging modalities.

To illustrate their relevance, two representative case studies are presented. In **Case A**, we analyze the behavior and convergence of the MLEM algorithm [7], using both conventional and newly introduced metrics to reveal subtle changes in image quality and reconstruction performance.

In **Case B**, we evaluate the novel RISE-1 algorithm, directly benchmarking it against MLEM using the same identical data, phantoms and reference images. This comparison highlights the ability of the proposed method to sensitively detect differences in reconstruction quality—both globally and within selected Regions of Interest (RoIs)—providing insights beyond those offered by traditional single-value measures.

As noted in Section 2.4.1, our analysis considered a broader family of global scalar and geometric comparison metrics—including information divergences and optimal-transport distances—that can offer enhanced sensitivity in high-fidelity regimes. For the sake of methodological consistency and clarity in the comparative studies that follow, we report exclusively the chi-square statistic in this section, even though more advanced metrics were examined in parallel.

3.1. CASE A: Exploring convergence and properties of MLEM

In this first case, we chose to show-case the method using a 2-D software phantoms (Shepp-Logan: Table 1 and Figure 1). The sinograms were generated using 128 equally spaced projections by simulating the emission and propagation of the photons with GEANT4/GATE using an “ideal collimator”; All simulated experiments were performed using controlled random seeds and identical instrument parameters to ensure reproducibility. Data generation and pre-processing settings were kept constant across all evaluations. To assess robustness, all reconstructed images were generated with comparable count statistics consistent with the Poisson processes governing γ -ray emission. Under these conditions, the MLEM algorithm demonstrated stable performance with only minor variations. For the case of Shepp-Logan a number of MLEM reconstructions were produced, each resulting from a different number of iterations. Four of them are shown in Figure 6, alongside the “Ideal Image” and their corresponding sinograms. Metric uncertainties were estimated using the Jackknife method [39–41]. The evaluation results are presented in Tables 5 and 6, in which four MLEM reconstructions are evaluated. Table 5 compares the MLEM reconstructions to the image of the “Ideal Image”, and Table 6 compares the “Ideal Sinogram” with those derived from the reconstructions through forward projection. The metrics for comparison of reconstruction with “Source Image” and “Ideal Image” are provided in Table 7.

Comparison of reconstructed image with “Ideal Image”				
Metric	MLEM (3 iterations)	MLEM (9 iterations)	MLEM (24 iterations)	MLEM (48 iterations)
NMSE	0.164 ± 0.003	0.050 ± 0.002	0.014 ± 0.002	0.009 ± 0.001
PSNR	14.728 ± 0.007	19.924 ± 0.008	29.656 ± 0.008	35.027 ± 0.006
CC	0.973 ± 0.001	0.980 ± 0.001	0.993 ± 0.001	0.998 ± 0.001
CNR	2.44 ± 0.006	2.89 ± 0.007	3.60 ± 0.008	4.113 ± 0.008
Luminance	1.000 ± 0.001	1.000 ± 0.001	1.000 ± 0.001	1.000 ± 0.001
Contrast	0.941 ± 0.001	0.998 ± 0.001	1.000 ± 0.001	1.000 ± 0.001
Structure	0.946 ± 0.008	0.974 ± 0.008	0.993 ± 0.008	0.995 ± 0.008
SSIM	0.890 ± 0.008	0.974 ± 0.008	0.993 ± 0.008	0.995 ± 0.008
SCI	0.575 ± 0.005	0.151 ± 0.002	0.057 ± 0.001	0.0119 ± 0.0004
$\chi^2_{red.}^1$	25.9	10.6	2.7	2.2

Table 5. Metrics resulting from the comparison of the Reconstructed Images of MLEM (with 3, 9, 24 and 48 (converged) iterations) to the “Ideal Reconstructed” Image.

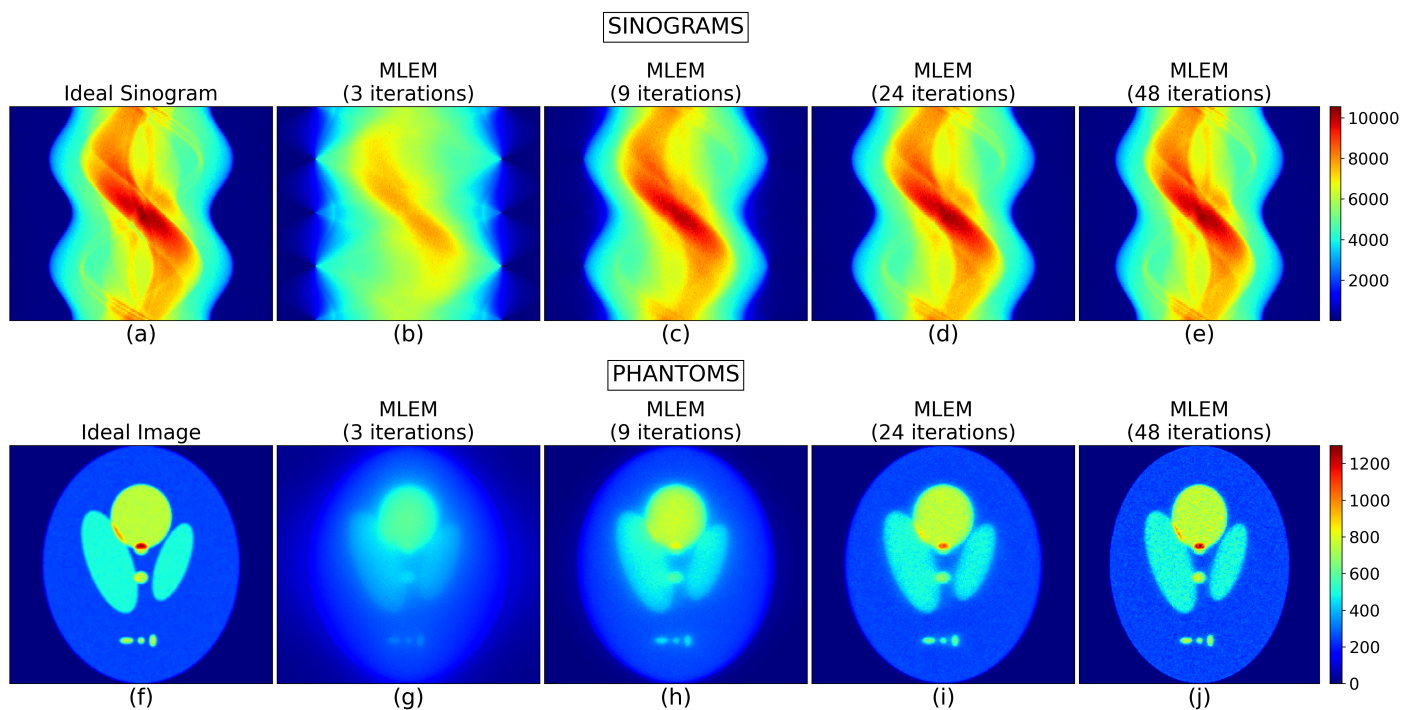


Figure 6. The top row depicts the "Ideal Sinogram" (a) and those resulting from different stages of MLEM (3, 9, 24, and 48 iterations) (b–e). The bottom row shows the "Ideal Image" (f) and the corresponding MLEM reconstructions (g–j).

Comparison of Sinograms corresponding to the "Ideal" and Reconstructed Images				
Metric	MLEM (3 iterations)	MLEM (9 iterations)	MLEM (24 iterations)	MLEM (48 iterations)
NMSE	0.10 ± 0.03	0.007 ± 0.008	0.001 ± 0.004	0.001 ± 0.003
PSNR	18.0 ± 0.2	32.2 ± 0.2	38.9 ± 0.2	41.8 ± 0.2
CC	0.982 ± 0.009	0.998 ± 0.004	0.999 ± 0.002	1.000 ± 0.001
CNR	1.7 ± 0.1	2.0 ± 0.1	2.0 ± 0.1	2.0 ± 0.1
Luminance	1.000 ± 0.001	1.000 ± 0.001	1.000 ± 0.001	1.000 ± 0.001
Contrast	0.97 ± 0.03	1.000 ± 0.003	1.000 ± 0.001	1.000 ± 0.001
Structure	0.96 ± 0.2	1.00 ± 0.2	1.0 ± 0.2	1.0 ± 0.2
SSIM	0.9 ± 0.2	0.99 ± 0.2	1.0 ± 0.2	1.00 ± 0.2
SCI	0.43 ± 0.04	0.06 ± 0.01	0.009 ± 0.004	0.003 ± 0.001
$\chi^2_{red.}^1$	122.0	12.1	3.6	1.9

Table 6. Metrics resulting from the comparison of the Sinograms of MLEM (with 3, 9, 24 and 48 (converged) iterations) to the "Ideal" sinogram.

In Tables 5 and 6 we notice that the metrics reflect the improvement of the image as the number of iterations increases and approaches convergence. The NMSE, SCI and $\chi^2_{red.}$ are decreasing, while the PSNR, CC, CNR and SSIM are increasing. We observe that SSIM on the image achieve a very high value after just 3 iterations, despite the images being significantly inferior to the converged version (Figure 6). This occurs because crucial image details—such as the boundaries between areas with different intensities and small hot spots—represent only a small fraction of the overall image, resulting in a limited impact on the overall metrics. We observe -see Table 7- that metrics comparing the reconstructed images to the "Ideal" Image indicate closer agreement than to the "Source" for Shepp-Logan phantom,

¹ χ^2 values use variances taken from MC counting statistics; pixel correlations are present and χ^2 is used as a discrepancy measure, not for error propagation.

Comparison of MLEM (48 iterations) reconstruction to "Source" and "Ideal" Reconstructed images		
Metric	Source	Ideal
NMSE	0.021 ± 0.001	0.009 ± 0.001
PSNR	32.904 ± 0.006	35.027 ± 0.006
CC	0.995 ± 0.001	0.998 ± 0.001
CNR	4.11 ± 0.09	4.11 ± 0.09
Luminance	1.000 ± 0.001	1.000 ± 0.001
Contrast	1.00 ± 0.001	1.000 ± 0.001
Structure	0.999 ± 0.008	0.995 ± 0.008
SSIM	0.989 ± 0.008	0.995 ± 0.008
SCI	0.0509 ± 0.0008	0.0119 ± 0.0004
χ^2_{red}	4.1	2.2

Table 7. Metrics resulting from the comparison of the Shepp-Logan phantom reconstructed with MLEM (full convergence). The first column provides the comparison with the “source” phantom image, and the second with the “ideal” reconstructed image.

as expected. Similar results and conclusions were obtained in a study for the Jaszczak phantom. When the SSIM in the comparison to the “Ideal Reconstructed” Image reaches the value of unity (1), it is supposed to indicate saturation, and therefore no consequent improvements can be achieved by further developing the algorithm. Additionally, we note that the sinograms after a few iterations closely resemble the experimental one, even though the images still have significant room for improvement. However, it is evident by a simple visual inspection of the corresponding images that this is not the case. This highlights a)the importance of evaluating the image itself when assessing a reconstruction technique, rather than focusing solely on the sinogram; this is possible only in studies with digital (software) or hardware phantoms, and b)the need of introducing new metrics in this near saturation - high fidelity regime such as the Structure and Contrast Index (SCI) which shows the expected behavior.

3.1.1. χ^2 and Difference Maps for sinograms and images:

As discussed in Section 2.4.2, difference maps and χ^2 maps provide further insight into the quality of reconstructions, highlighting both absolute deviations and statistically normalized ones respectively. In this case study, we apply these diagnostics to evaluate MLEM reconstructions at two stages: after 9 and 48 iterations, as illustrated in Figure 7. Notably, in the fully converged case, the χ^2 map of the sinogram ($\chi^2_{red.} = 2$) shows minimal residual structure, indicating convergence, indicating that minimal additional information can be extracted from the data. By contrast, the maps obtained after 9 iterations ($\chi^2_{red.} = 12$) reveal clear residual patterns, underscoring that the reconstruction has not yet converged and it has not captured the available information. The difference maps (Fig. 7), in contrast to the χ^2 maps, also provide the sign of the discrepancy in each area, allowing us to identify which regions in the image and sinogram are overestimated or underestimated. In the difference map of the MLEM image after 9 iterations, we notice that the background around the hot spots is significantly overestimated, while the boundaries of the hot spots are underestimated—an effect that is greatly mitigated after 48 iterations.

3.1.2. Structure Contrast Index (SCI) of images and sinograms:

Structure Contrast Index (SCI) is the metric we introduced to quantify the magnitude of the discrepancy seen in the difference maps of sinograms and images. The values of SCI for images and sinograms for all the stages of MLEM are given in Table 8. SC and SSIM

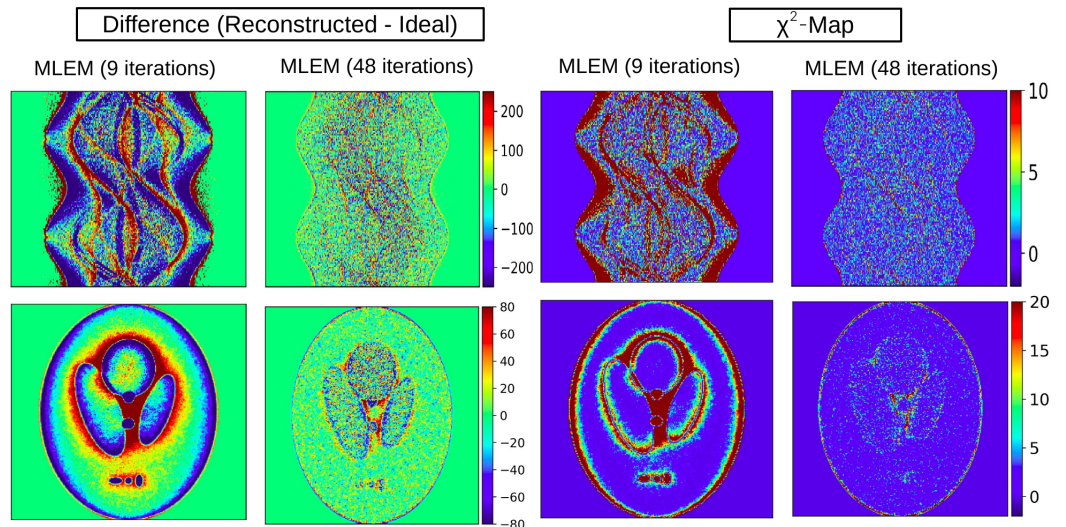


Figure 7. The first two rows on the left provide the difference and χ^2 maps for the image and sinogram, for the MLEM reconstruction after 9 iterations. The last two columns on the right show the same maps for the case of MLEM after 48 iterations. The difference and χ^2 maps reveal areas of the images that are not well-represented by the reconstruction.

components evaluation given in Table 5 and 6 are illustrated in Figure 8. As expected, the SCI of the difference between the sinogram for MLEM (3 iterations) is higher compared to the case of MLEM at full convergence. As the algorithm converges, the difference becomes dominated by statistical fluctuation and noise, leading to a lower SCI for both images and sinograms, indicating that little additional information can be obtained from the experimental data.

Metric	MLEM (3 iterations)	MLEM (9 iterations)	MLEM (24 iterations)	MLEM (48 iterations)
SSIM (sinogram)	0.000 ± 0.007	0.0000 ± 0.0007	0.0000 ± 0.0004	0.0000 ± 0.0002
SSIM (image)	0.000 ± 0.003	0.0000 ± 0.0001	0.0000 ± 0.0001	0.0000 ± 0.00006
Luminance (sinogram)	0.000 ± 0.006	0.000 ± 0.002	0.000 ± 0.002	0.000 ± 0.002
Luminance (image)	0.000 ± 0.002	0.0000 ± 0.0002	0.0000 ± 0.0004	0.0000 ± 0.0002
Contrast (sinogram)	0.58 ± 0.05	0.16 ± 0.03	0.07 ± 0.02	0.05 ± 0.02
Contrast (image)	0.696 ± 0.001	0.424 ± 0.001	0.234 ± 0.001	0.192 ± 0.001
Structure (sinogram)	0.738 ± 0.007	0.349 ± 0.005	0.130 ± 0.004	0.063 ± 0.001
Structure (image)	0.826 ± 0.007	0.356 ± 0.005	0.242 ± 0.003	0.062 ± 0.002
SCI (sinogram)	0.43 ± 0.04	0.06 ± 0.01	0.009 ± 0.003	0.003 ± 0.001
SCI (image)	0.575 ± 0.005	0.151 ± 0.002	0.057 ± 0.001	0.0119 ± 0.0004

Table 8. SSIM, Luminance, Contrast, Structure and SCI values of sinogram and image difference maps (reconstructed – ideal) using MLEM at different iteration stages. For each metric, the first row corresponds to sinogram values and the second row to image values.

3.1.3. Intensity Spectrum of Images and Sinograms

We have introduced the intensity spectrum analysis of tomographic images and their corresponding sinograms as an additional diagnostic tool.

In Figure 9, we study the image and sinogram spectra for several MLEM stages (3, 9, 24, and 48 iterations). In addition we show the utility of this tool investigating how the number of angular projections used in reconstruction affects image quality (Figure 10). A Shepp-Logan phantom, simulated using an "ideal collimator," serves as the ground

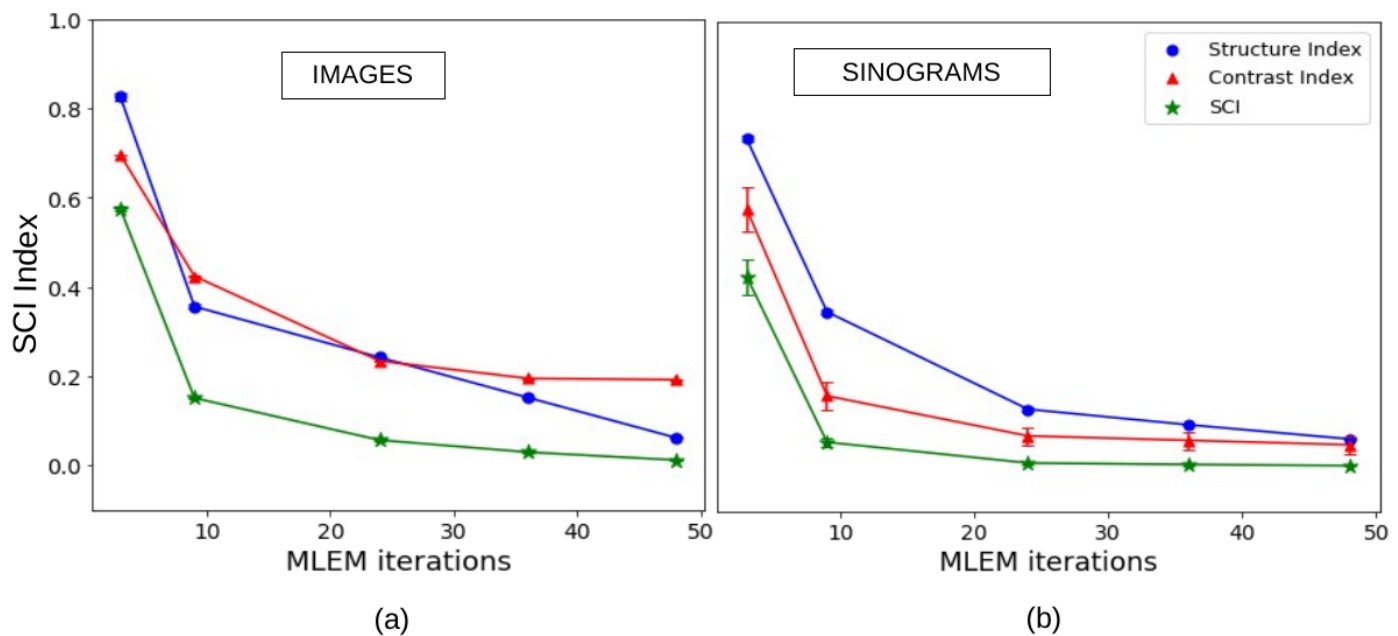


Figure 8. a) Convergence of the SCI index of the difference between the reconstructed and "Ideal Image", relative to the "Ideal" as the number of MLEM iterations increases. b) Convergence of the SCI index of the difference between the sinogram resulted from a reconstruction and the "Ideal Sinogram", relative to the "Ideal" for the four stages of MLEM.

truth. Reconstructions were performed using sinograms with 32, 64, and 256 uniformly distributed planar projection.

In Figure 10, we present the intensity spectra of the "Ideal Image" and those of the reconstructed images for each projection set. As the number of projections increases, the spectral peaks in the reconstructed images become narrower, progressively converging toward the spectrum of the "Ideal Image". This demonstrates and quantifies that increased angular sampling enhances the reconstruction's ability to recover accurate intensity distributions, particularly around localized high-intensity regions (e.g., "hot spots"), resulting in higher resolution. Interestingly, Figure 10, which displays the intensity spectra of the corresponding sinograms, shows that the overall spectral shape of the sinograms remains rather insensitive to the number of projections. This indicates that while the information content of the sinogram may appear similar, the resolution and fidelity of the final reconstructed image are significantly influenced by the density of angular sampling. The image spectra capture with greater sensitivity than sinogram-based metrics alone.

In the next example (Figure 11), we present the intensity spectra of reconstructed images and sinograms obtained from different levels of statistics. Artifacts during reconstruction -because of statistical fluctuation on the sinograms that allow the migration of image intensity to neighboring pixels- contribute to the distortion of the spectrum. Higher levels of statistics lead to sharper peaks on the spectrum.

The two examples shown demonstrate that the intensity spectrum analysis is a valuable diagnostic tool for assessing reconstruction quality. In addition, the spectrum of the sinograms shows that no area with different numbers of counts reaching the detector is missed or underestimated. It is important to analyze both the sinograms and the images, as agreement in the sinogram's spectrum does not guarantee the agreement in the image's spectrum.

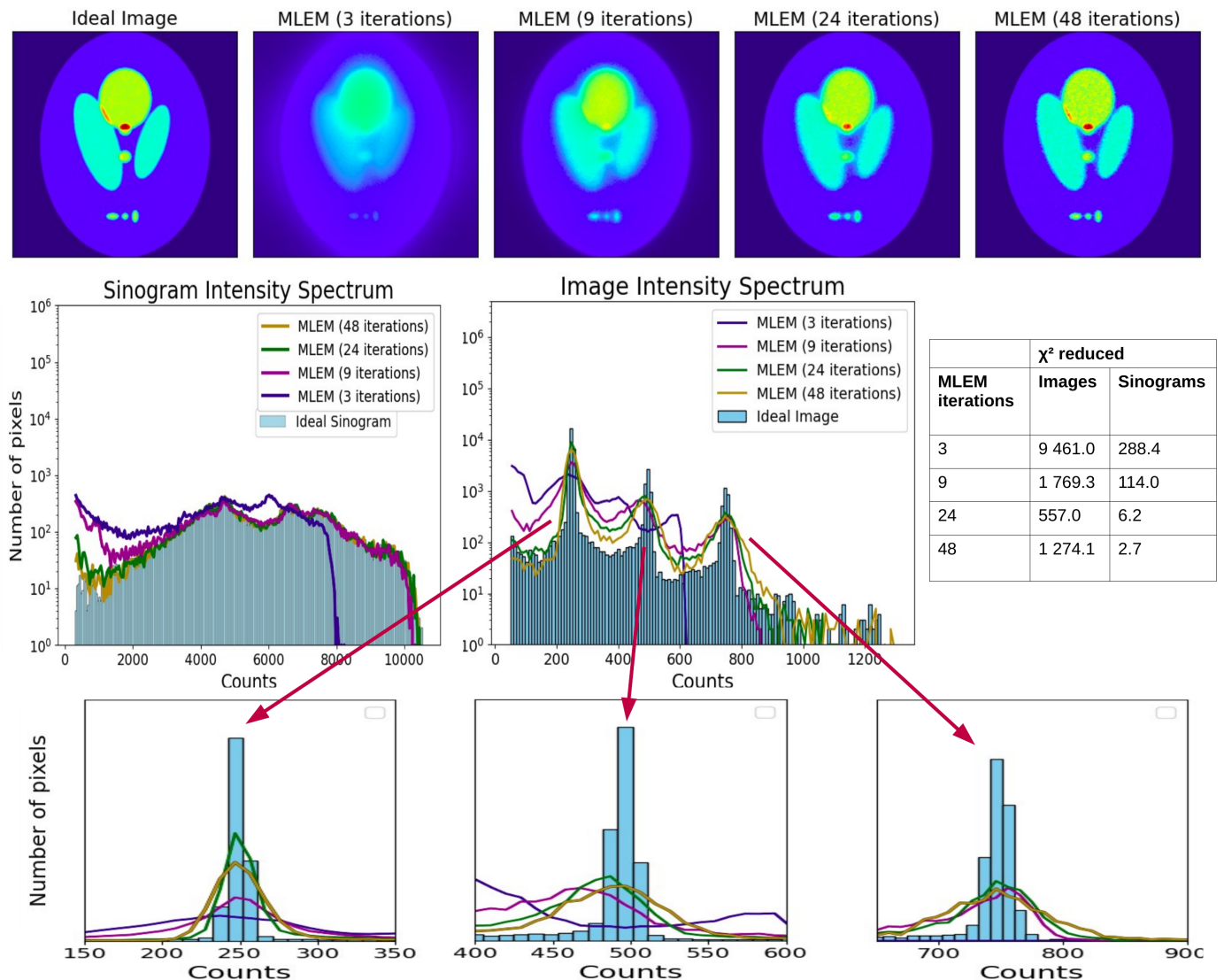


Figure 9. The top row of the figure displays the "Ideal Image" alongside the four MLEM reconstructions. In the second row, the spectra of the "Ideal Image" and each of the four reconstructions are illustrated on the left. On the right, the spectra of the "Ideal Sinogram" and those resulting from MLEM are presented.

3.1.4. Region-of-Interest (RoI) Analysis: Application of new Metrics and Images

A limitation of global evaluation metrics—such as χ^2 or SSIM—is that they dilute the effect of localized discrepancies across the full image or sinogram. As a result small but diagnostically critical deviations (e.g., missed hot spots, poor edge delineation) may go undetected. To remedy this, as discussed in section 2.4.3, we make use of the well known technique of Region-of-Interest (RoI) analysis [27–33] in conjunction with the newly introduced images and metrics.

We defined in Section 2.4.3 (see Figure 1) three representative RoIs in the Shepp-Logan phantom to target specific reconstruction challenges: For each of these RoIs, we compute localized χ^2 values, spectral intensity distributions, and SSIMs of the reconstructed and reference images or sinograms. These localized metrics offer a powerful complement to global scores, as they reveal details that may go unnoticed otherwise.

In Figure 12 we present the RoIs of the "Ideal Image" alongside those from the four MLEM reconstructions. The results, presented in Table 9 and Figure 14, demonstrate that

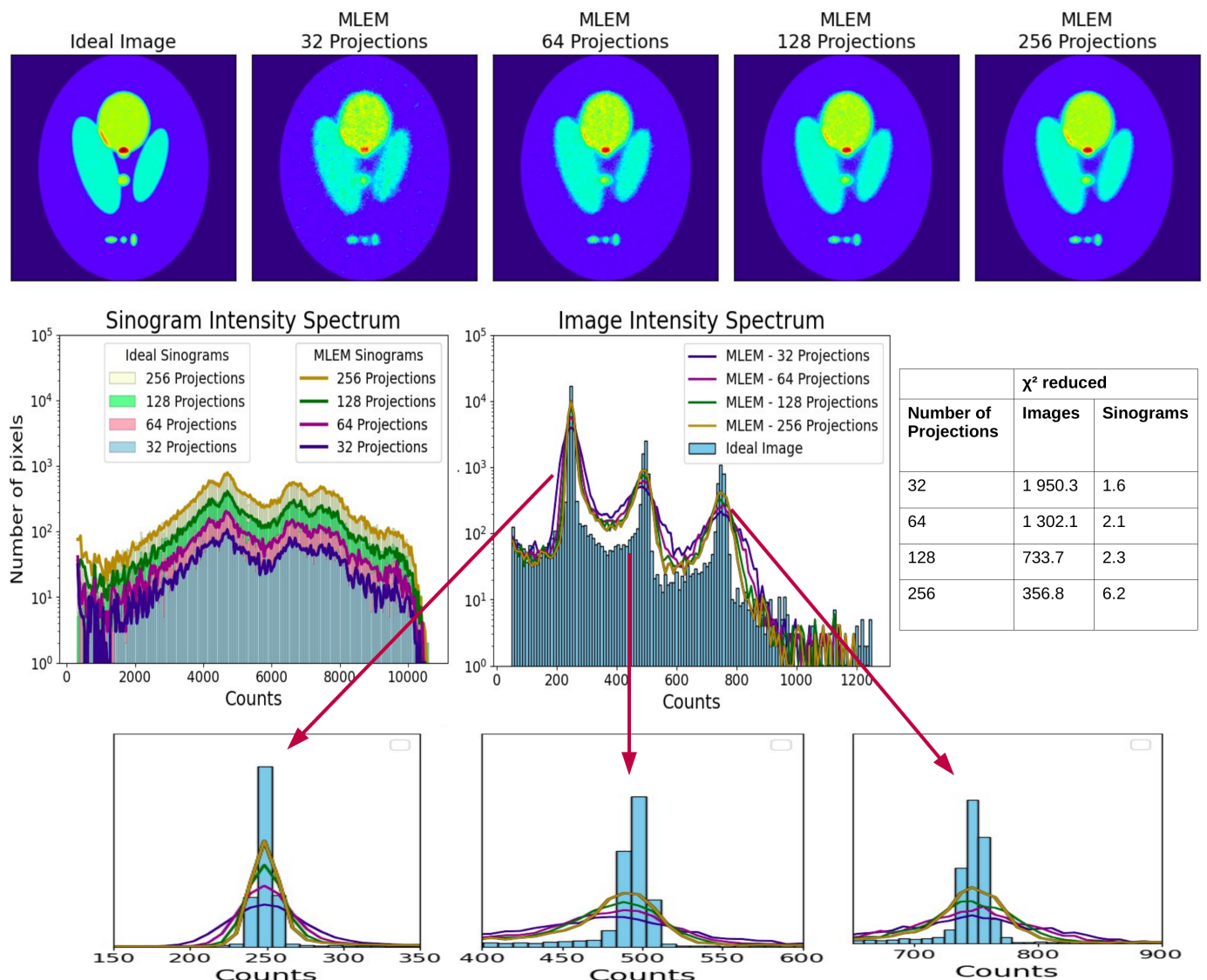


Figure 10. The top row of the figure displays the "Ideal Image" alongside the three reconstructions from MLEM at full convergence, and with 32, 64, and 256 projections. In the second row, the spectra of the "Ideal Image" and each of the three reconstructions are illustrated on the left. On the right, the spectra of the "Ideal Sinogram" and those resulting from 32, 64, and 256 projections are presented.

ROI-specific metrics provide a more granular view of reconstruction quality compared to global metrics. For example, SSIM values for ROIs are significantly lower than those computed for the entire image, emphasizing the importance of localized evaluation in identifying performance gaps. Additionally, the Structure and Contrast Index (SCI) values for ROIs showed greater variation across MLEM iterations, and substantially higher values, about an order of magnitude, indicative of its sensitivity, as illustrated in Figure 13, further underscoring the utility of ROI analysis in tracking convergence and identifying areas for improvement.

By leveraging ROI analysis in conjunction with the new metrics, we validate the sensitivity and interpretability of the proposed metrics and tools, demonstrating their ability to characterize local image fidelity and optimize reconstruction methods.

3.2. CASE B: Benchmarking a new reconstruction method

In this second demonstration case, we apply the new method to evaluate and benchmark the performance of RISE-1 (Section 2.4.4), a novel algorithmic reconstruction method.

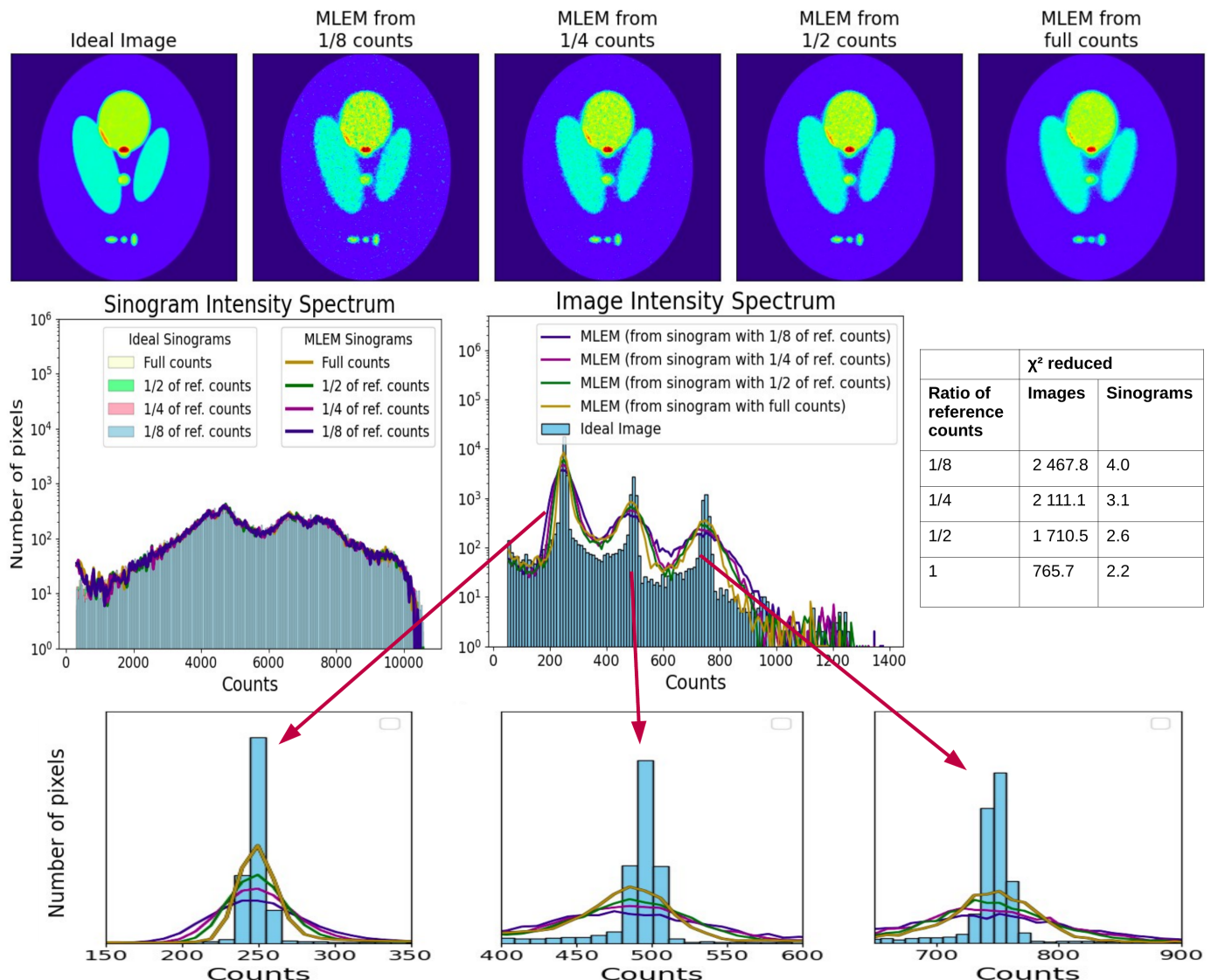


Figure 11. The top row of the figure displays the "Ideal Image" alongside the four reconstructions from MLEM at full convergence, utilizing sinograms with different level of statistics (1/8, 1/4, 1/2 and full counts). In the second row, the spectra of the "Ideal Image" and each of the four reconstructions are illustrated on the left. On the right, the spectra of the "Ideal Sinograms" with of the four cases are presented.

Using the introduced images and quantitative metrics, we compare the performance of the novel RISE-1 against the established MLEM method.

The proposed methodology treats the algorithm as a "black box"—its internal logic, whether proprietary, unpublished, or incomprehensible, is immaterial. What matters is the output: how accurately and reliably the method reconstructs the image. This approach ensures that benchmarking remains fair, consistent, and broadly applicable to any reconstruction method, regardless of its complexity or transparency.

To demonstrate this benchmarking process, we selected a particularly challenging test case: the reconstruction of a Shepp-Logan phantom with significant background activity. The specific activity ratio across regions (background : side ellipses : central ellipse and hotspots) is set to (20 : 5 : 10), according to Table 1. The "Ideal Sinograms" were generated using the "ideal collimator" model, ensuring a high-quality reference dataset for evaluation.

Figure 15 shows MLEM and RISE-1 reconstructions alongside the "Ideal Image" and their corresponding sinograms. By visually examining the resulting images produced by

Comparison of MLEM Reconstructions for Different ROIs and Entire Image					
Metric	MLEM (3 iterations)	MLEM (9 iterations)	MLEM (24 iterations)	MLEM (48 iterations)	MLEM (48 iterations)
RoI-1					Entire Image
NMSE	0.9 \pm 0.1	0.49 \pm 0.08	0.14 \pm 0.04	0.031 \pm 0.027	0.009 \pm 0.001
PSNR	6.9 \pm 0.1	11.6 \pm 0.1	22.1 \pm 0.4	26.6 \pm 0.4	35.027 \pm 0.006
CC	0.91 \pm 0.09	0.97 \pm 0.04	0.99 \pm 0.02	0.99 \pm 0.01	0.998 \pm 0.001
CNR	3.01 \pm 0.04	4.28 \pm 0.05	5.69 \pm 0.06	7.29 \pm 0.07	4.114 \pm 0.008
Luminance	0.99 \pm 0.04	1.00 \pm 0.01	1.000 \pm 0.001	1.000 \pm 0.001	1.000 \pm 0.001
Contrast	0.2 \pm 0.1	0.60 \pm 0.09	0.94 \pm 0.04	0.999 \pm 0.007	1.000 \pm 0.001
Structure	0.82 \pm 0.05	0.93 \pm 0.06	0.97 \pm 0.07	0.99 \pm 0.07	0.995 \pm 0.008
SSIM	0.19 \pm 0.03	0.56 \pm 0.03	0.91 \pm 0.06	0.98 \pm 0.07	0.995 \pm 0.008
SCI	0.99 \pm 0.07	0.93 \pm 0.07	0.58 \pm 0.06	0.10 \pm 0.02	0.0118 \pm 0.0002
RoI-2					Entire Image
NMSE	1.1 \pm 0.2	0.53 \pm 0.05	0.23 \pm 0.04	0.11 \pm 0.06	0.009 \pm 0.001
PSNR	8.6 \pm 0.3	11.7 \pm 0.3	19.6 \pm 0.4	24.7 \pm 0.3	35.027 \pm 0.006
CC	0.8 \pm 0.1	0.94 \pm 0.06	0.97 \pm 0.03	0.95 \pm 0.04	0.998 \pm 0.001
CNR	1.60 \pm 0.02	2.34 \pm 0.05	2.83 \pm 0.06	3.17 \pm 0.06	4.114 \pm 0.008
Luminance	0.99 \pm 0.03	1.000 \pm 0.007	1.000 \pm 0.001	1.000 \pm 0.001	1.000 \pm 0.001
Contrast	0.30 \pm 0.09	0.59 \pm 0.04	0.88 \pm 0.03	0.99 \pm 0.02	1.000 \pm 0.001
Structure	0.59 \pm 0.03	0.88 \pm 0.06	0.94 \pm 0.06	0.95 \pm 0.06	0.995 \pm 0.008
SSIM	0.17 \pm 0.02	0.52 \pm 0.05	0.83 \pm 0.06	0.94 \pm 0.06	0.995 \pm 0.008
SCI	0.98 \pm 0.07	0.93 \pm 0.07	0.70 \pm 0.06	0.33 \pm 0.06	0.0118 \pm 0.0002
RoI-3					Entire Image
NMSE	1.08 \pm 0.03	0.29 \pm 0.01	0.108 \pm 0.006	0.058 \pm 0.004	0.009 \pm 0.001
PSNR	9.45 \pm 0.02	12.13 \pm 0.02	21.97 \pm 0.02	27.94 \pm 0.02	35.027 \pm 0.006
CC	0.899 \pm 0.007	0.939 \pm 0.005	0.977 \pm 0.003	0.985 \pm 0.002	0.998 \pm 0.001
CNR	0.508 \pm 0.006	0.949 \pm 0.008	1.788 \pm 0.008	2.364 \pm 0.008	4.114 \pm 0.008
Luminance	0.977 \pm 0.004	1.000 \pm 0.001	1.000 \pm 0.001	1.000 \pm 0.001	1.000 \pm 0.001
Contrast	0.601 \pm 0.007	0.907 \pm 0.007	0.980 \pm 0.004	0.999 \pm 0.001	1.000 \pm 0.001
Structure	0.798 \pm 0.008	0.879 \pm 0.008	0.955 \pm 0.008	0.971 \pm 0.007	0.995 \pm 0.008
SSIM	0.469 \pm 0.006	0.797 \pm 0.008	0.936 \pm 0.008	0.970 \pm 0.008	0.995 \pm 0.008
SCI	0.93 \pm 0.01	0.68 \pm 0.01	0.398 \pm 0.007	0.139 \pm 0.003	0.0118 \pm 0.0002

Table 9. The metrics (MSE, NMSE, PSNR, CC, SSIM and CNR) for each ROI.

the two algorithms (MLEM and RISE-1), we observe equivalent performance and similarly accurate outcomes. Both algorithms successfully capture the overall structure and correctly reveal all hotspots, providing a faithful representation of the phantom. However, when focusing on the three ROIs, differences in performance emerge. Figure 16 displays the ROIs from each reconstruction, and the Figure 17 presents the values of the metrics (Table 10) in graphical form which are also shown in Table 10 along with the derived uncertainties. We notice that, for all three ROIs, the small hot spots are better reproduced in the RISE-1 reconstruction than in MLEM. This is also reflected in the higher values of CC, SSIM, and CNR, and the lower NMSE achieved with RISE-1. We observe that the newly introduced SCI index shows by far the highest discriminating power as it can be seen in Table 10 and Figure 14. None of the metrics applied over the entire image can capture these fine differences.

In Figure 19 the difference and χ^2 maps of the image and sinogram, for RISE-1 and MLEM reconstructions are provided. In both cases the chi-square map contains low values approaching the statistical fluctuation level, without clear structure, indication of the excellent performance of both methods of reconstruction.

The SCI of the value of the difference (RISE-1 - Ideal) and (MLEM - Ideal) for the each image and sinogram are very low also reflecting the excellence of both methods. However, in the corresponding ROIs (Figure 18), the resulting SCI values are significantly higher, indicating that there is still room for improvement.

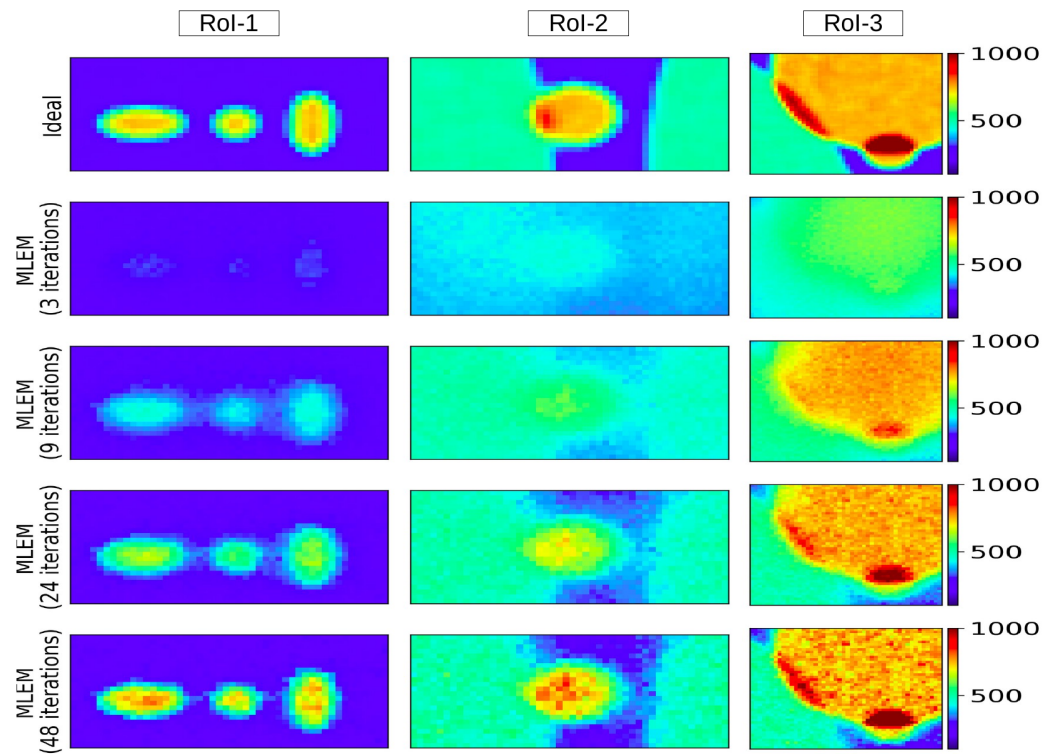


Figure 12. The three Shepp-Logan RoIs shown for the "Ideal Image" and the Reconstructed Images from four stages of MLEM.

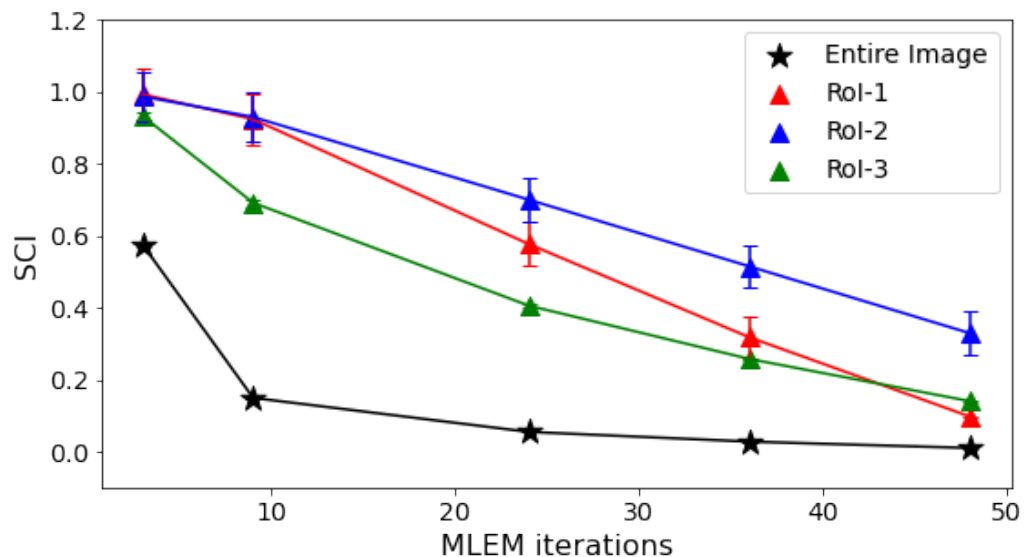


Figure 13. Convergence of the SCI index for the difference between the reconstructed and the "Ideal Image" (RoIs 1, 2, and 3), relative to the "Ideal Image," as MLEM converges.

In addition, we present the spectra of the reconstructed image with RISE-1, for both image (Figure 20 (a) and (c)) and sinogram (Figure 20 (b) and (d)) and we compare them with MLEM. In Figure 20 (a) and (c) the black line (RISE-1 image) poorly follows the peaks of the "Ideal Image" (blue bars), with a narrower width compared to MLEM (blue line), showing that RISE-1 outperforms MLEM in imaging areas with sharp intensity changes. Their performance can be quantified by measuring the resulting $\chi^2_{reduced}$ of each reconstruction bunched marked vs the "Ideal Image's" spectrum the resulting values are shown in the figure (MLEM $\chi^2_{reduced}=1778$ and $\chi^2_{reduced}=1170$). In Figure 20 (b and d) we

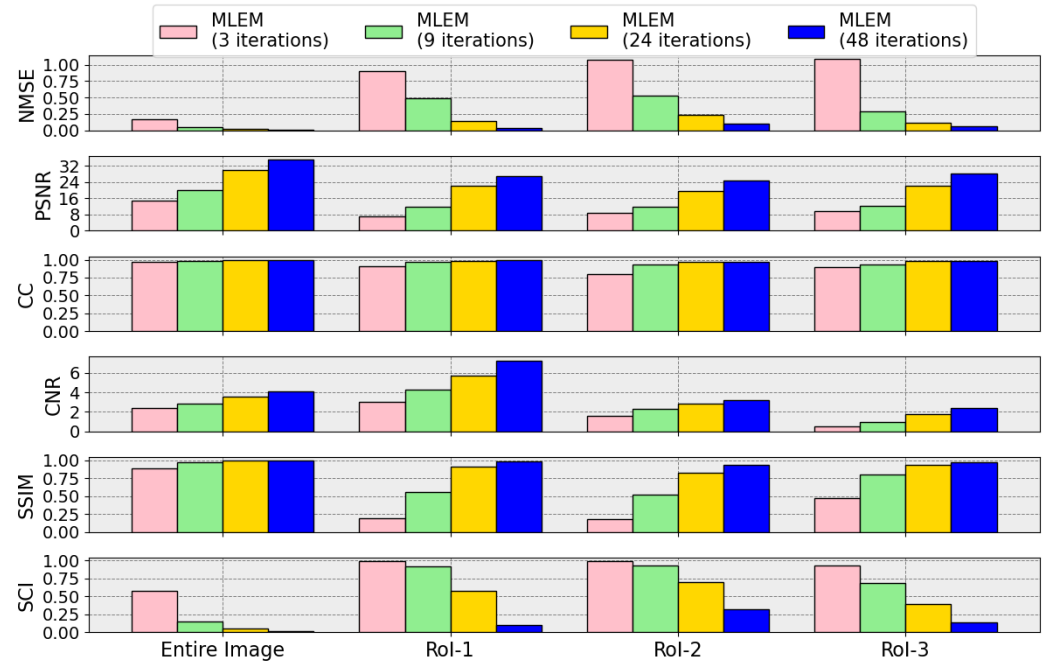


Figure 14. A selection of metrics (NMSE, PSNR, CC, SSIM, CNR and SCI) are presented for each one of the RoIs and the entire image, and for four different stages of MLEM evolution.

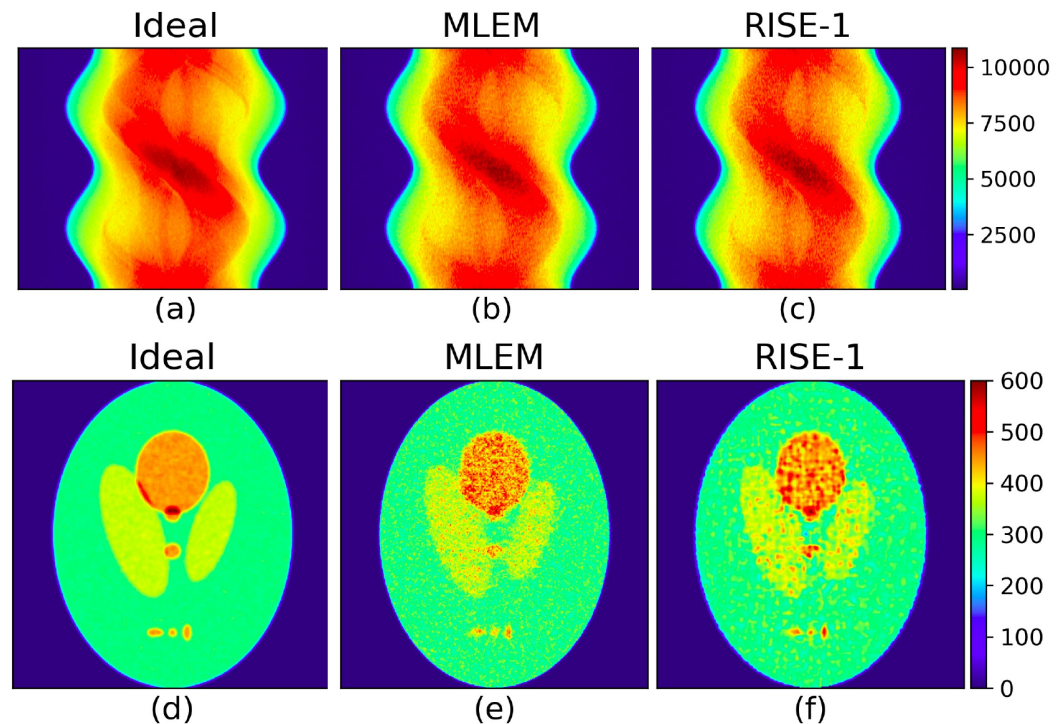


Figure 15. (a) "Ideal Sinogram", (b) MLEM reconstruction, (c) RISE-1 reconstruction, (d) "Ideal image", (e) MLEM reconstruction, (f) RISE-1 reconstruction

observe that the spectra of the MLEM and RISE-1 sinograms are almost identical. The $\chi^2_{reduced}$ value of RISE-1 ($\chi^2_{reduced}=3.45$), is lower than the one of MLEM ($\chi^2_{reduced}=5.15$).

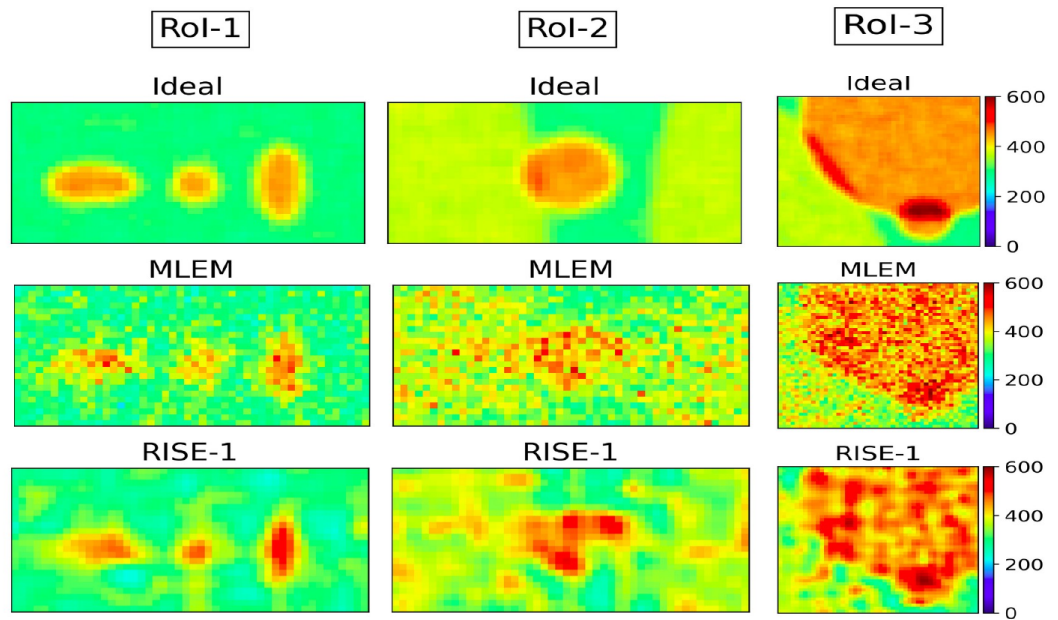


Figure 16. The panels (a-c) present the three ROIs from the Ideal phantom. The panels (d-f) and (g-i) show the corresponding areas reconstructed using MLEM and RISE-1, respectively.

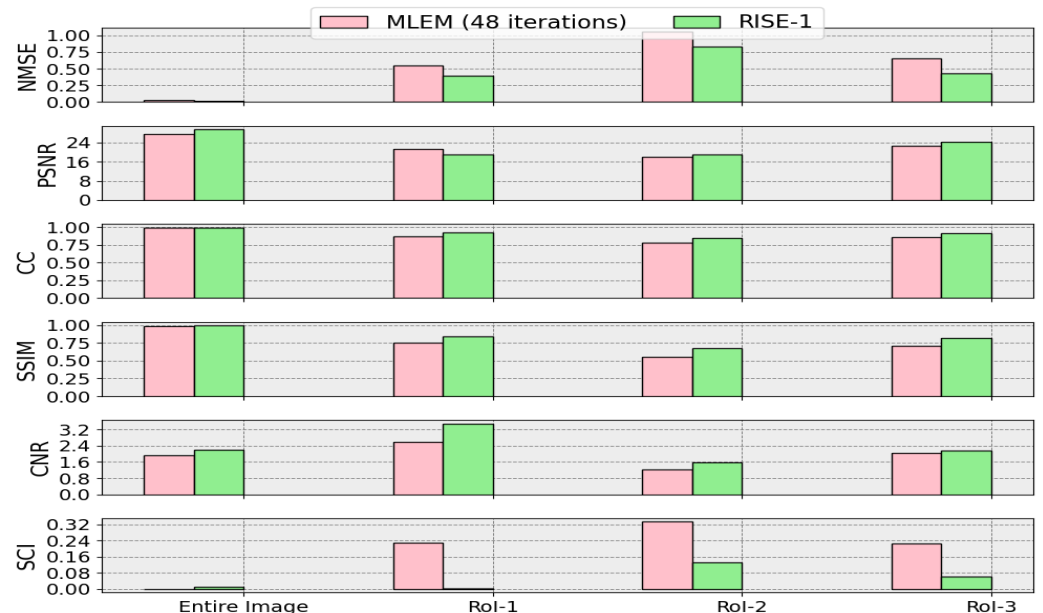


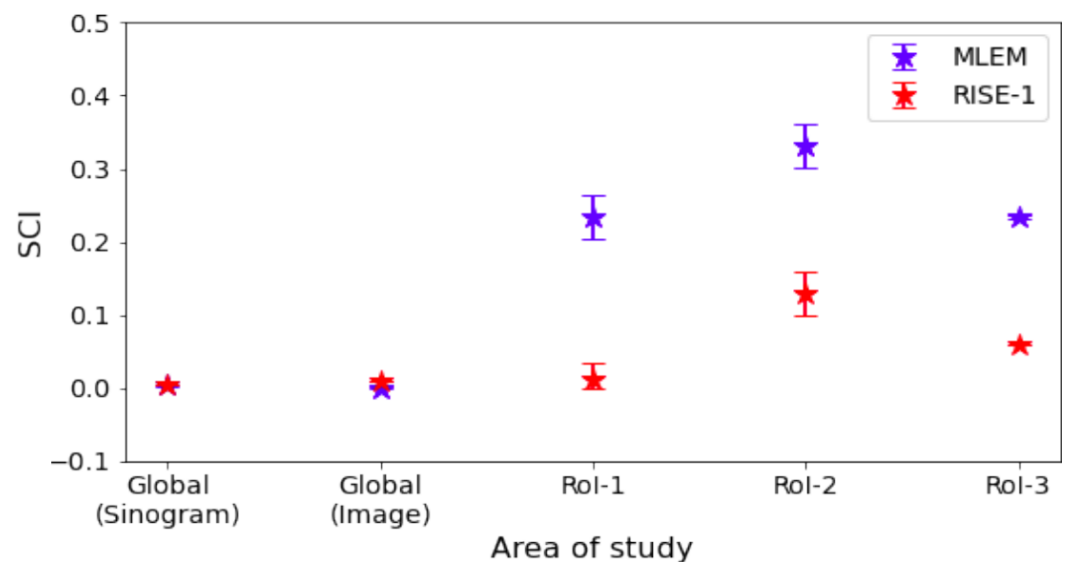
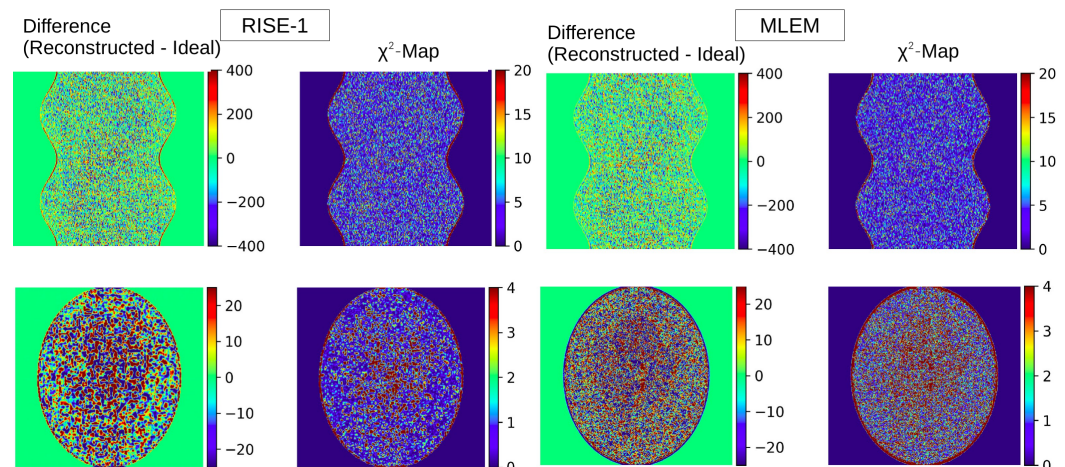
Figure 17. The metrics NMSE, PSNR, CC, CNR, SSIM and SCI are presented for each one of the ROIs and the entire image, across the two different reconstruction techniques: MLEM and RISE-1.

4. Applicability to Hardware Phantoms and Field Data

Although this study has focused on software phantoms, the proposed evaluation framework applies equally well to hardware phantoms and to a lesser degree to field data, including clinical imaging cases.

For hardware phantoms, only minimal adjustments are needed when applying standardized reference images and diagnostic metrics. Such phantoms are well-characterized (e.g., Jaszczak or IEC phantoms commonly used in nuclear medicine), the "Ideal" and "Realistic" images can be generated using high precision simulation codes and then follow the same methodology as the one used for software phantoms. These can then be incorpo-

Metric	Entire Image		RoI-1		RoI-2		RoI-3	
	MLEM	RISE-1	MLEM	RISE-1	MLEM	RISE-1	MLEM	RISE-1
NMSE	0.024 ± 0.001	0.014 ± 0.001	0.5 ± 0.1	0.4 ± 0.1	1.1 ± 0.2	0.83 ± 0.16	0.66 ± 0.02	0.43 ± 0.01
PSNR	27.574 ± 0.006	29.514 ± 0.005	21.3 ± 0.2	19.1 ± 0.3	18.07 ± 0.07	19.0 ± 0.2	22.69 ± 0.03	24.23 ± 0.01
CC	0.994 ± 0.001	0.996 ± 0.001	0.88 ± 0.05	0.92 ± 0.05	0.78 ± 0.07	0.85 ± 0.06	0.859 ± 0.007	0.913 ± 0.005
SSIM	0.988 ± 0.008	0.993 ± 0.008	0.75 ± 0.05	0.84 ± 0.06	0.55 ± 0.04	0.68 ± 0.05	0.713 ± 0.007	0.817 ± 0.008
CNR	1.935 ± 0.003	2.211 ± 0.003	2.57 ± 0.05	3.47 ± 0.06	1.25 ± 0.04	1.56 ± 0.05	2.058 ± 0.008	2.163 ± 0.008
SCI	0.001 ± 0.001	0.0096 ± 0.0002	0.23 ± 0.03	0.004 ± 0.023	0.33 ± 0.03	0.13 ± 0.03	0.226 ± 0.003	0.063 ± 0.001

Table 10. Comparison of metrics across Entire Image and ROIs for MLEM and RISE-1.**Figure 18.** The values of SCI for different areas (Sinogram, Global Image, RoI-1, RoI-2 and RoI-3), for MLEM and RISE-1 reconstructions.**Figure 19.** Top row: The difference map (reconstruction - "Ideal") and χ^2 -map on the sinogram space, for RISE-1 (left) and MLEM (right). Bottom row: The difference map (reconstruction - "Ideal") and χ^2 -map on the image space, for RISE-1 (left) and MLEM (right).

rated into performance benchmarking protocols, particularly during system calibration, acceptance testing, or routine quality assurance.

Extending the framework to clinical or experimental data introduces additional constraints, chiefly because the true object is generally unknown. In such cases, many of the pixel (voxel)-level image comparisons used in simulations cannot be applied directly. Instead, meaningful analysis can still be carried out by comparing measured sinograms

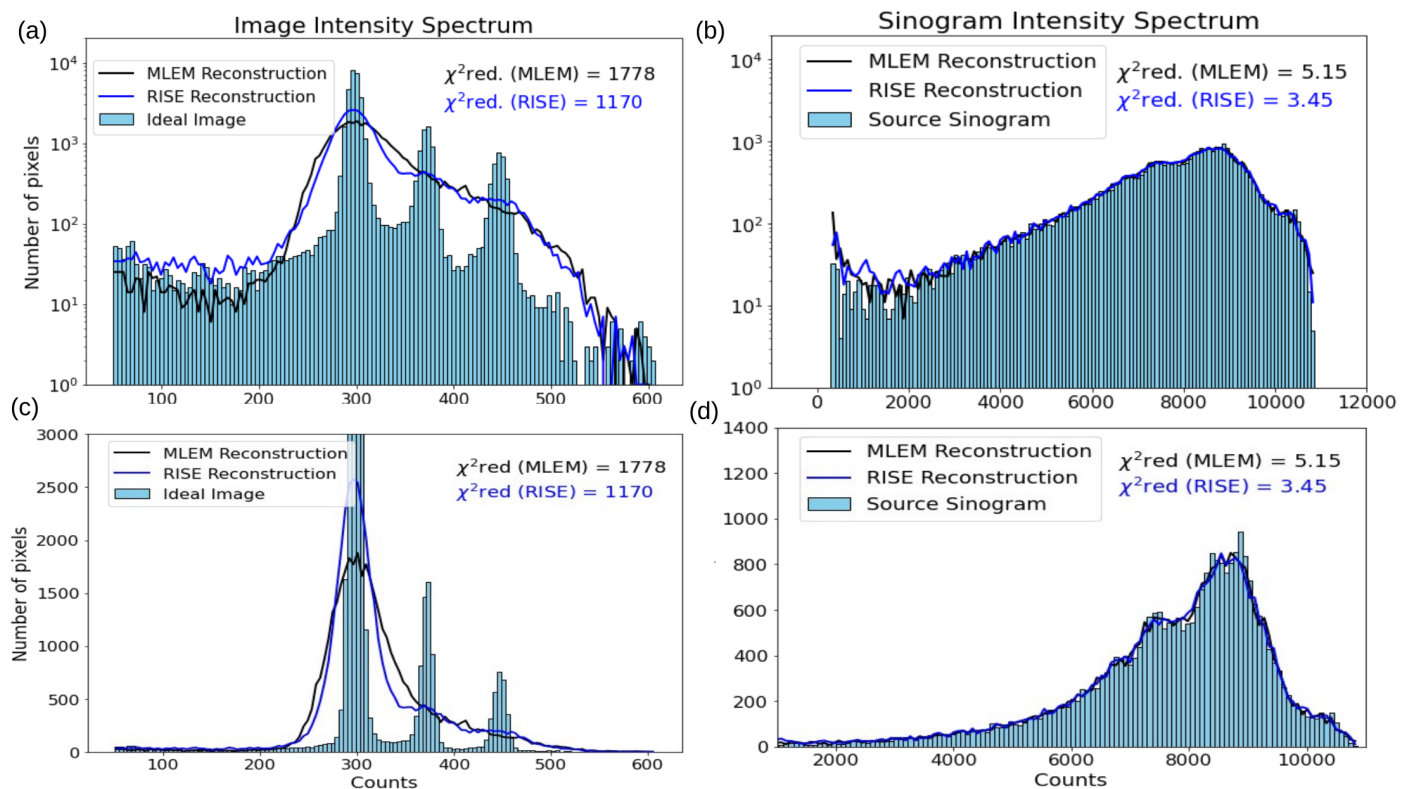


Figure 20. On the left: the spectra of "Ideal Image" (blue bars), MLEM (blue line) and RISE-1 reconstruction (black line). On the right: The spectra of source sinogram (blue bars) and the ones resulted from MLEM (blue line) and RISE-1 reconstructions (black line).

with those re-projected from reconstructed images. Metrics such as difference and χ^2 maps, difference sinograms, and frequency-domain spectral comparisons remain informative in this context.

To illustrate the applicability and importance of the proposed framework of metrics to the case of clinical data we processed a DATSCAN SPECT (using a I-123 bases radio-pharmaceutical) of a patient suffering from Parkinson's disease, for which no CT-based attenuation map was available. Initially, a preliminary reconstruction was performed without attenuation correction. Subsequently, a uniform water region was introduced into the attenuation map to approximate photon attenuation effects, including both photoelectric absorption and Compton scattering. This enabled reconstruction using two approaches: (a) a purely geometric projection matrix without attenuation modeling, and (b) a full attenuation-corrected model simulated using the GATE/GEANT package. Figure 21 present the reconstructed images and their corresponding sinograms for the two approaches.

Quantitative evaluation was performed by comparing the reconstructed sinograms to the detector sinograms, and the results are summarized in Table 11. It is evident from

Metric	Without Attenuation Correction (NC)	With Attenuation Correction (AC)
NMSE	0.085 ± 0.006	0.067 ± 0.003
PSNR	21.1 ± 0.3	24.19 ± 0.19
CC	0.9880 ± 0.0006	0.9916 ± 0.0003
CNR	2.16 ± 0.07	2.31 ± 0.07
SSIM	0.9642 ± 0.0001	0.9715 ± 0.0001
SCI	0.2606 ± 0.0003	0.2773 ± 0.0002

Table 11. Comparison of reconstruction metrics between no attenuation correction (NC) and attenuation correction (AC) cases using a selection of single valued metrics.

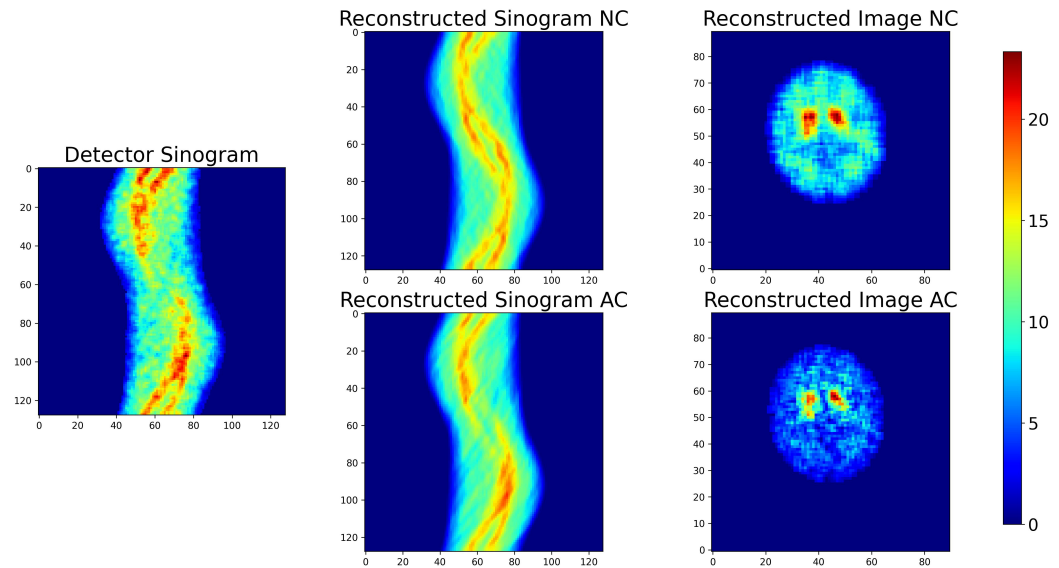


Figure 21. Left: Detector sinogram. Top row: Reconstructed image and sinogram without attenuation correction (AC). Bottom row: Reconstructed image and sinogram with attenuation correction (NC).

the table, the metrics obtained using attenuation correction a (AC) are generally better, with PSNR emerging as the most sensitive. The χ^2 and difference maps (Figure 22) provide a more detailed view. They clearly indicate that the AC sinogram matches the detector

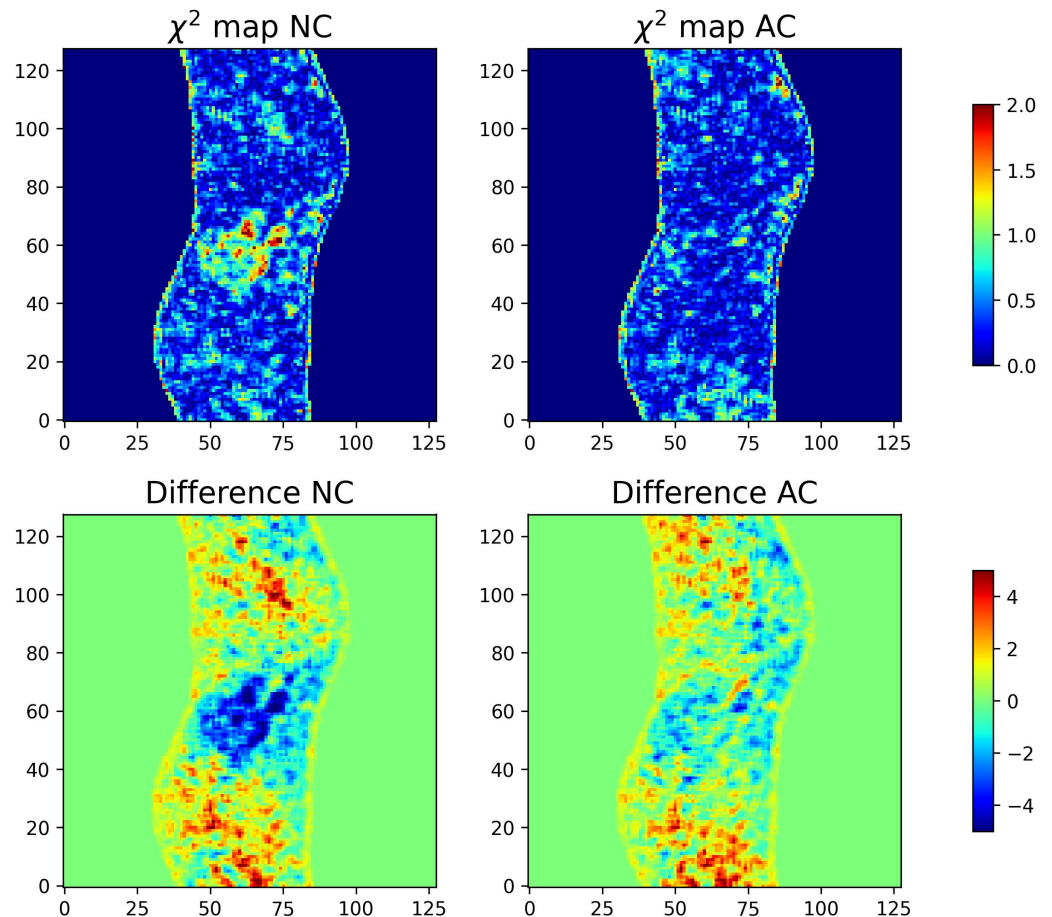


Figure 22. Top row: χ^2 maps comparing the reconstructed sinograms to the detector sinograms for both cases NC and AC. Bottom row: Difference maps comparing the reconstructed sinograms to the detector sinograms for both cases NC and AC.

sinogram more accurately, especially in the central region. In contrast, the NC case exhibits a considerable discrepancy in the same area, which corresponds to the region of maximum radiotracer concentration. This highlights the efficacy of the attenuation correction method. The benefits of this approach are expected to be even more pronounced when accurate attenuation maps are available from joint SPECT/CT acquisitions.

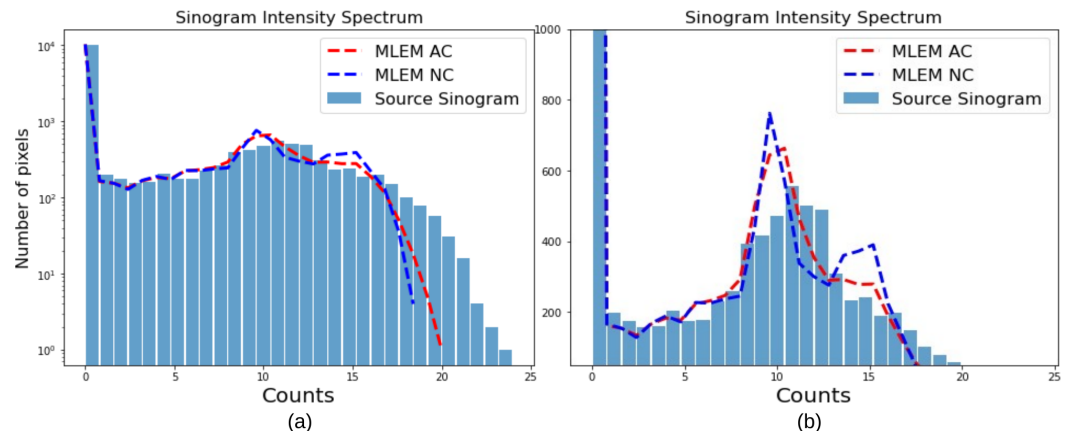


Figure 23. Sinogram intensity spectra of the detector data and the reconstructed sinograms with and without attenuation correction. Panel (a) shows the spectra on a logarithmic scale, and panel (b) on a linear scale.

Even in clinical settings, where ground truth is not directly available, the proposed evaluation framework provides a structured approach to evaluate reconstruction performance. It can be used to check internal consistency, identify regions of the sinogram that are inadequately accounted for, and assess the stability of reconstructions under real acquisition conditions. When a phantom or a high-fidelity synthetic substitute is available, comparisons between "Realistic" reconstructions and their Ideal counterparts can reveal performance losses attributable to physical limitations.

In addition to sinogram-based diagnostics, certain metrics can still be meaningfully applied directly on reconstructed images, even when no ground-truth reference is available. A particularly relevant example is the Contrast-to-Noise Ratio (CNR), provided that the analysis is restricted to well-defined anatomical or functional regions. To demonstrate this point, we evaluated the reconstructed DATSCAN images of the Parkinsonian patient discussed above by defining a Region-of-Interest (RoI) around the striatal uptake and estimating the background using the area outside the selected RoI. Although this procedure does not require a reference "Ideal Image", it offers a practical measure of detectability and contrast recovery in real clinical data.

Figure 24 illustrates the reconstructed images obtained without and with attenuation correction, together with the selected RoI (red box). The CNR (Figure 24) was computed independently for each case using the reconstructed intensities only. The attenuation-corrected reconstruction exhibits a significantly higher CNR, consistent with the improved contrast observed visually and with the sinogram-based metrics reported earlier. This example highlights that, even in the absence of ground-truth information, the proposed framework accommodates complementary image-domain metrics that retain interpretability and clinical relevance.

These capabilities highlight the framework's versatility, making it valuable not only for algorithm development but also for practical system evaluation and the optimization of clinical imaging protocols.

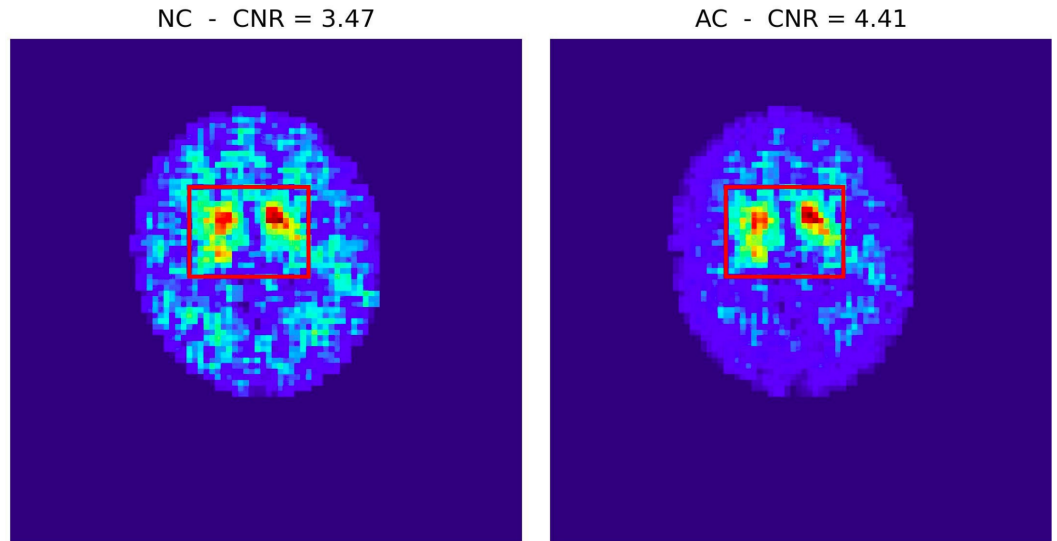


Figure 24. Reconstructed DATSCAN SPECT images of a Parkinsonian patient without attenuation correction (NC) (left) and with attenuation correction (AC) (right). The red rectangle indicates the Region-of-Interest (RoI) used for calculating the Contrast-to-Noise Ratio (CNR) directly from the reconstructed images. Since no ground-truth phantom exists for clinical data, the CNR was estimated using the mean activity inside the RoI and the noise level derived from the surrounding background region. The AC reconstruction demonstrates a markedly improved CNR (NC: 3.47, AC: 4.41), consistent with the enhanced visual contrast and with the quantitative improvements observed in the corresponding sinogram-domain metrics.

5. Conclusions

Traditional global metrics such as SSIM, PSNR, CC, and NMSE saturate early and fail to detect residual structure in the high-fidelity regime increasingly reached by modern reconstruction methods. This limitation motivates the need for a more sensitive and physically grounded evaluation framework. The present work addresses this need through a structured set of standardized reference images and sinograms and a hierarchy of diagnostic metrics operating in image, sinogram, and spectral domains.

We introduced a family of reference images—Source, Detector, Ideal, and Realistic—that represent distinct stages of the imaging and reconstruction pipeline. These images provide physically meaningful anchors for evaluating reconstruction fidelity and form a consistent basis for comparing algorithms and acquisition conditions across modalities. We also developed diagnostic tools that quantify discrepancies at multiple levels, including spatial difference maps, χ^2 maps, RoI-based comparisons, and the Structure–Contrast Index (SCI). Together, these tools provide a coherent, multi-domain system for assessing reconstruction quality.

The case studies demonstrate the sensitivity and coherence of this framework in the regime of high-fidelity reconstructions. In the analysis of MLEM convergence and in the comparison of RISE-1 with MLEM, RoI-based metrics, χ^2 maps, and SCI identified structured residuals long after global metrics had saturated. Difference-spectra analysis provided a complementary view in the intensity domain, revealing changes in resolution and local contrast not visible in pixel-wise diagnostics; its role is to quantify discrepancies in the distribution of intensities, not to characterize spatial structure. The same methodology extends to hardware phantoms and, with appropriate restrictions, to clinical data. In clinical and experimental settings, where ground truth is unavailable, sinogram-domain

comparisons, spectral diagnostics, and RoI-based measures remain informative and directly applicable to image-quality assurance and protocol optimization.

Future work will include the study of spectral-domain metrics in three-dimensional phantoms, refinement of residual-information measures beyond χ^2 , development of multi-modal phantoms, and evaluation under low-statistics acquisition conditions. Integration with deep-learning reconstruction pipelines and automated RoI selection are promising directions. Importantly, the methodology will be validated using hardware phantoms to establish its robustness under realistic acquisition conditions.

Taken together, the evaluation framework introduced here provides a unified, physics-grounded, and diagnostically sensitive approach for assessing tomographic reconstruction quality. By combining standardized images with multi-domain diagnostic tools—including RoIs, SCI, and spectral metrics—it enables rigorous, reproducible comparison of reconstruction methods from simulation and algorithm development through to clinical practice.

Author Contributions: Conceptualization, CNP; software, AF, ES and TL; formal analysis, AF, ES and TL; writing—original draft preparation, CNP and AF; writing—review and editing, CNP, AF, ES and TL; supervision, CNP; funding acquisition, TL. All authors have read and agreed to the published version of the manuscript.

Funding: The work was supported by The Cyprus Institute, the Cyprus Academy of Sciences, Letters and Arts, and the Cyprus Research and Innovation Foundation under the project PERSPECT (Project No. EXCELLENCE/0524/0410), implemented within the Cohesion Policy Programme “THALIA 2021–2027” and co-funded by the European Union.

Acknowledgments: This work was supported by The Cyprus Institute under the medical imaging group.

Conflicts of Interest: The authors declare no conflicts of interest.

Abbreviations

The following abbreviations are used in this manuscript:

χ^2	Chi-square statistic
AC	Attenuation Correction
AI	Artificial Intelligence
CC	Correlation Coefficient
CNR	Contrast to Noise Ratio
CT	Computed Tomography
GATE	Geant4 Application for Tomographic Emission
JS	Jensen–Shannon divergence
KL	Kullback–Leibler divergence
MLEM	Maximum Likelihood Expectation Maximization
MRI	Magnetic Resonance Imaging
NB	Number of histogram bins (spectral analysis)
NC	No Attenuation Correction
NMSE	Normalized Mean Square Error
PET	Positron Emission Tomography
PSNR	Peak Signal to Noise Ratio
RISE-1	Reconstructed Image from Simulations Ensemble – 1
RoI	Region of Interest
SCI	Structure and Contrast Index
SPECT	Single Photon Emission Tomography
SSIM	Structural Similarity Index Measure

References

1. Tassiopoulou, S.; Koukiou, G.; Anastassopoulos, V. Algorithms in Tomography and Related Inverse Problems—A Review. *Algorithms* **2024**, *17*. <https://doi.org/10.3390/a17020071>.
2. Bhadra, S.; Kelkar, V.A.; Brooks, F.J.; Anastasio, M.A. On Hallucinations in Tomographic Image Reconstruction. *IEEE Transactions on Medical Imaging* **2021**, *40*, 3249–3260. <https://doi.org/10.1109/TMI.2021.3077857>.
3. Collins, D.; Zijdenbos, A.; Kollokian, V.; Sled, J.; Kabani, N.; Holmes, C.; Evans, A. Design and construction of a realistic digital brain phantom. *IEEE Transactions on Medical Imaging* **1998**, *17*, 463–468. <https://doi.org/10.1109/42.712135>.
4. Ghaly, M.; Du, Y.; Fung, G.S.K.; Tsui, B.M.W.; Links, J.M.; Frey, E. Design of a digital phantom population for myocardial perfusion SPECT imaging research. *Physics in Medicine & Biology* **2014**, *59*, 2935. <https://doi.org/10.1088/0031-9155/59/12/2935>.
5. Harries, J.; Jochimsen, T.H.; Scholz, T.; et al. A realistic phantom of the human head for PET-MRI. *EJNMMI Physics* **2020**, *7*, 52. <https://doi.org/10.1186/s40658-020-00320-z>.
6. Pullens, P.; Roebroeck, A.; Goebel, R. Ground truth hardware phantoms for validation of diffusion-weighted MRI applications. *Journal of Magnetic Resonance Imaging (JMRI)* **2010**, *32*, 482–488. <https://doi.org/10.1002/jmri.22243>.
7. Hwang, D.; Zeng, G.L. Convergence study of an accelerated ML-EM algorithm using bigger step size. *Physics in Medicine & Biology* **2005**, *51*, 237. <https://doi.org/10.1088/0031-9155/51/2/004>.
8. Shepp, L.A.; Logan, F.D. The Fourier Reconstruction of a Head Section. *IEEE Transactions on Nuclear Science* **1974**, *21*, 21–43.
9. Gach, H.M.; Tanase, C.; Boada, F. 2D & 3D Shepp-Logan Phantom Standards for MRI. In Proceedings of the 2008 19th International Conference on Systems Engineering, 2008, pp. 521–526. <https://doi.org/10.1109/ICSEng.2008.15>.
10. Jan, S.; Santin, G.; Strul, D.; Staelens, S.; Assié, K.; Autret, D.; Avner, S.; Barbier, R.; Bardies, M.; Bloomfield, P.M.; et al. GATE: a simulation toolkit for PET and SPECT. *Physics in Medicine and Biology* **2004**, *49*, 4543–4561. <https://doi.org/10.1088/0031-9155/49/19/007>.
11. Sarrut, D.; Arbor, N.; Baudier, T.; Borys, D.; Etxebeste, A.; Fuchs, H.; Gajewski, J.; Grevillot, L.; Jan, S.; Kagadis, G.C.; et al. The OpenGATE ecosystem for Monte Carlo simulation in medical physics. *Physics in Medicine and Biology* **2022**, *67*, 10.1088/1361-6560/ac8c83. <https://doi.org/10.1088/1361-6560/ac8c83>.
12. Radon, J. On the determination of functions from their integral values along certain manifolds. *IEEE Transactions on Medical Imaging* **1986**, *5*, 170–176. <https://doi.org/10.1109/TMI.1986.4307775>.
13. Seynaeve, P.C.; Broos, J.I. De historiek van de tomografie [The history of tomography]. *Journal belge de radiologie* **1995**, *78*, 284–8.
14. Hill, D.L.G.; Batchelor, P.G.; Holden, M.; Hawkes, D.J. Medical image registration. *Physics in Medicine and Biology* **2001**, *46*, R1–R45. <https://doi.org/10.1088/0031-9155/46/3/201>.
15. Schober, P.; Boer, C.; Schwarte, L.A. Correlation Coefficients: Appropriate Use and Interpretation. *Anesthesia & Analgesia* **2018**, *126*, 1763–1768. <https://doi.org/10.1213/ANE.0000000000002864>.
16. Wang, Z.; Bovik, A.C. Mean squared error: Love it or leave it? A new look at Signal Fidelity Measures. *IEEE Signal Processing Magazine* **2009**, *26*, 98–117. <https://doi.org/10.1109/MSP.2008.930649>.
17. Horé, A.; Ziou, D. Image Quality Metrics: PSNR vs. SSIM. In Proceedings of the 2010 20th International Conference on Pattern Recognition, Istanbul, Turkey, 2010; pp. 2366–2369. <https://doi.org/10.1109/ICPR.2010.579>.
18. Geissler, A.; Gartus, A.; Foki, T.; Tahamtan, A.R.; Beisteiner, R.; Barth, M. Contrast-to-noise ratio (CNR) as a quality parameter in fMRI. *Journal of Magnetic Resonance Imaging (JMRI)* **2007**, *25*, 1263–1270. <https://doi.org/10.1002/jmri.20935>.
19. Wang, Z.; Bovik, A. A universal image quality index. *IEEE Signal Processing Letters* **2002**, *9*, 81–84. <https://doi.org/10.1109/97.995823>.
20. Lin, J. Divergence measures based on Shannon entropy. *IEEE Transactions on Information Theory* **1974**, *22*, 106–110.
21. Endres, D.M.; Schindelin, J.E. A new metric for probability distributions. *IEEE Transactions on Information Theory* **2003**, *49*, 1858–1860.

22. Kullback, S.; Leibler, R.A. On Information and Sufficiency. *Annals of Mathematical Statistics* **1951**, *22*, 79–86.
23. Le Cam, L.M. *Asymptotic Methods in Statistical Decision Theory*; Springer: New York, NY, USA, 1986.
24. Villani, C. *Optimal Transport: Old and New*; Springer: Berlin/Heidelberg, Germany, 2009.
25. Peyré, G.; Cuturi, M. Computational Optimal Transport: With Applications to Data Science. *Foundations and Trends in Machine Learning* **2019**, *11*, 355–607. <https://doi.org/10.1561/2200000073>.
26. Flamary, R.; Courty, N.; et al. POT: Python Optimal Transport Library (Updated). *Journal of Machine Learning Research* **2021**, *22*, 1–8.
27. Setio, A.A.A.; Ciompi, F.; Litjens, G.; Gerke, P.; Jacobs, C.; van Riel, S.J.; Wille, M.M.W.; Naqibullah, M.; Sánchez, C.I.; van Ginneken, B. Pulmonary Nodule Detection in CT Images: False Positive Reduction Using Multi-View Convolutional Networks. *IEEE Transactions on Medical Imaging* **2016**, *35*, 1160–1169. <https://doi.org/10.1109/TMI.2016.2536809>.
28. Poldrack, R.A. Region of interest analysis for fMRI. *Social Cognitive and Affective Neuroscience* **2007**, *2*, 67–70. <https://doi.org/10.1093/scan/nsm006>.
29. Doukas, C.; Maglogiannis, I. Region of Interest Coding Techniques for Medical Image Compression. *IEEE Engineering in Medicine and Biology Magazine* **2007**, *26*, 29–35. <https://doi.org/10.1109/EMB.2007.901793>.
30. Pandey, D.; Yin, X.; Wang, H.; Su, M.Y.; Chen, J.H.; Wu, J.; Zhang, Y. Automatic and fast segmentation of breast region-of-interest (ROI) and density in MRIs. *Helijon* **2018**, *4*, e01042. <https://doi.org/10.1016/j.heliyon.2018.e01042>.
31. Amakusa, S.; Matsuoka, K.; Kawano, M.; et al.. Influence of region-of-interest determination on measurement of signal-to-noise ratio in liver on PET images. *Annals of Nuclear Medicine* **2018**, *32*, 1–6. <https://doi.org/10.1007/s12149-017-1215-y>.
32. Schain, M.; Varnäs, K.; Cselényi, Z.; et al.. Evaluation of Two Automated Methods for PET Region of Interest Analysis. *Neuroinformatics* **2014**, *12*, 551–562. <https://doi.org/10.1007/s12021-014-9233-6>.
33. Jiang, C.F.; Chang, C.C.; Huang, S.H. Regions of interest extraction from SPECT images for neural degeneration assessment using multimodality image fusion. *Multidimensional Systems and Signal Processing* **2012**, *23*. <https://doi.org/10.1007/s11045-011-0162-3>.
34. Shepp, L.A.; Vardi, Y. Maximum Likelihood Reconstruction for Emission Tomography. *IEEE Transactions on Medical Imaging* **1982**, *1*, 113–122. <https://doi.org/10.1109/TMI.1982.4307558>.
35. Papanicolas, C.N.; Koutsantonis, L.; Stiliaris, E. A Novel Analysis Method for Emission Tomography, 2018, [arXiv:physics.med-ph/1804.03915].
36. Keliri, A.; Koutsantonis, L.; Stiliaris, E.; Parpottas, Y.; Charitou, G.; Panagi, S.; Papanicolas, C.N. Application of RISE in SPECT Myocardial Perfusion Imaging, using a Cardiac Phantom. In Proceedings of the 2021 IEEE Nuclear Science Symposium and Medical Imaging Conference (NSS/MIC), 2021, pp. 1–5. <https://doi.org/10.1109/NSS/MIC44867.2021.9875921>.
37. Koutsantonis, L.; Rapsomanikis, A.N.; Stiliaris, E.; Papanicolas, C.N. Examining an image reconstruction method in infrared emission tomography. *Infrared Physics & Technology* **2019**, *98*, 266–277. <https://doi.org/https://doi.org/10.1016/j.infrared.2019.03.015>.
38. Lemesios, C.; Koutsantonis, L.; Papanicolas, C.N. RISE: Tomographic Image Reconstruction in Positron Emission Tomography. In Proceedings of the 2019 IEEE Nuclear Science Symposium and Medical Imaging Conference (NSS/MIC), 2019, pp. 1–4. <https://doi.org/10.1109/NSS/MIC42101.2019.9060020>.
39. Busing, F.M.T.A.; Meijer, E.; van der Leeden, R. Delete-m Jackknife for Unequal m. *Statistics and Computing* **1999**, *9*, 3–8. <https://doi.org/10.1023/A:1008800423698>.
40. Quenouille, M.H. Notes on Bias in Estimation. *Biometrika* **1956**, *43*, 353–360. <https://doi.org/10.2307/2332914>.
41. Tukey, J.W. Bias and confidence in not-quite large samples. *The Annals of Mathematical Statistics* **1958**, *29*, 614. Abstract.